Czech Technical University in Prague

Faculty of Nuclear Sciences and Physical Engineering

Department of Physics

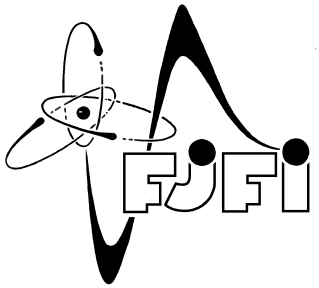

Diploma Thesis

ATLAS Forward Proton Project on the ATLAS Experiment

Author:

Bc. Oleksandr Korchak

Supervisor:

prom. fyz. Václav Vrba, CSc.

June 2013

ATLAS Forward Proton Project on the ATLAS Experiment

Author: Bc. Oleksandr Korchak

Supervisor: prom. fyz. Vaclav Vrba, CSc.

Key words: ATLAS, AFP project, 3D silicon detectors, test beam.

Abstract:

The goal of the ATLAS Forward Proton (AFP) project is to add a set of detectors on both sides of the ATLAS experiment at the LHC. The final setup will consist of two 3D pixel tracking detectors and one high-resolution time of flight detector. These detectors will be placed approximately 210 m from the interaction point (IP). The AFP detectors will allow identification of the forward protons produced at small angles. This will allow studies of Single Diffraction, Double Pomeron Exchange, Central Exclusive Production and photon-photon processes.

An extensive evaluation plan which includes device irradiation and beam tests is carried out in order to determine the performance of the 3D silicon setector prototypes for the AFP project. Two sensor technologies of 3D double sided-design sensors are currently (June 2013) being considered for the AFP project which are developed by the following institutes: National Microelectronics Center (CNM) and Fondazione Bruno Kessler (FBK).

In this thesis, the data analysis results from the AFP August 2012 testbeam at CERN and the AFP June 2013 testbeam at DESY are presented. During these testbeams, the 3D silicon sensors for the AFP project have been evaluated.

Project "ATLAS Forward Proton" na experimentu ATLAS

Autor:	Bc. Oleksandr Korchak
Vedoucí práce:	prom. fyz. Václav Vrba, CSc.

Klíčová slova:	ATLAS, AFP project, 3D křemíkové detektory, test beam.

Abstrakt:

Cílem projektu ATLAS Forward Proton (AFP) je rozšířit experiment ATLAS na urychlovači LHC o 2 sady detektorů po obou stranách. Po rozšíření bude experiment obsahovat dva 3D pixel tracking detektory a jeden time of flight detektor na každé straně přední oblasti. Tyto detektory budou umístěny ve vzdálenosti přibližně 210 m od srážkové oblasti a umožní studium jednoduché difrakce (difrakce na jedné štěrbině), double pomeron exchange, central exclusive production a foton-foton procesy.

V rámci projektu AFP bylo věnováno značné úsilí testování kvality prototypů křemíkových 3D sensorů, mimo jiné ozařováním a prováděním test beamů. V současné době (červen 2013) se uvažuje o dvou technologiích pro výrobu oboustranných 3D sensorů: CNM (National Microelectronics Center), vyrobené v Barceloně (Španělsko), a FBK (Fondazione Bruno Kessler), vyrobené v Trentu (Itálie).

Tato práce předkládá výsledky analýz test beamů AFP uskuteněných v srpnu 2012 v laboratoři CERN a v červnu 2013 v laboratoři DESY. Tyto test beamy měly za úkol prověřit kvalitu křemíkových 3D sensorů určených pro projekt AFP.

Prohlášení:

Prohlašuji, že jsem svou diplomovou práci vypracoval samostatně a použil jsem pouze podklady (literaturu, software, atd.) uvedené v přiloženém seznamu.

Nemám závažný důvod proti užití tohoto školního díla ve smyslu 60 Zákona .121/2000 Sb., o právu autorském, o právech souvisejících s právem autorským a o změně některých zákonů (autorský zákon).

V Praze dne

Acknowledgments

First of all, I would like to thank my supervisor Vaclav Vrba for his guidance throughout the preparation of this work. Also I would like to thank Michael Marcisovsky for help with language and factual corrections, and Igor Rubinsky for his consultations during data reconstruction.

Contents

Chapter 1

Introduction

The central exclusive production and photon-photon interactions in pp collisions are interesting processes to study at the LHC, the reasons are mensioned in Chapter 3. The theoretical uncertainties of these processes are quite large, thus the measurements of e.g. exclusive jets could lead to better understanding of the strong interaction which is ruling these processes. Possible results of these studies includes the determination of the Higgs boson quantum numbers and probing new physics via the gauge boson anomalous couplings.

In order to measure these processes, new dedicated detectors are necessary to tag the forward protons. The AFP project has been presented by the ATLAS Collaboration as an upgrade of the ATLAS detector. In the first phase, the design postulates installation of four stations on both sides of the central ATLAS detector. Each station will consist of a silicon detector measuring the proton impact position and a timing detector which measures the time of flight (TOF) of the scattered protons with picosecond precision. These detectors will be placed in the Hamburg movable beampipe to allow the adjustment of their horizontal position.

Currently (June 2013), the AFP project is considering two sensor technologies of 3D silicon double-sided design: CNM (National Microelectronics Center) made in Barcelona, Spain and FBK (Fondazione Bruno Kessler) made in Trento, Italy.

This thesis presents the results of beam tests of CNM and FBK 3D silicon detectors under the AFP conditions: small dead space at the edge of the sensors and non-uniform irradiation.

Chapter 2 gives a short overview of the ATLAS experiment and of the AFP project in particular. Chapter 3 describes the physics which can be studied with the help of the AFP detectors. Chapter 4 presents the basics of particle detection using semiconductor detectors and also an overview of novel 3D silicon sensors. The basic concepts of the test beam setup are presented in Chapter 5 together with the description of the data taking process and the list of testing configurations. Chapter 6 describes the offline data analysis performed by the Tbmon software and provides data analysis studies and summarizes the results. The conclusions of this thesis are presented in Chapter 7.

Chapter 2

The LHC Accelerator and the ATLAS Detector

2.1 The LHC

The Large Hadron Collider (LHC), the world's largest and most powerful particle accelerator. The LHC consists of a 27-kilometre ring of superconducting magnets with a number of accelerating structures to boost the energy of the particles along the way (see Figure 2.1). Inside the accelerator, two high-energy particle beams travel at close to the speed of light before they are made to collide. The beams travel in opposite directions in separate beam pipes – two tubes kept at ultrahigh vacuum. They are guided around the accelerator ring by a strong magnetic field maintained by superconducting electromagnets. The electromagnets are built from coils of special electric cable that operates in a superconducting state, efficiently conducting electricity without resistance or loss of energy.

Seven experiments at the Large Hadron Collider (LHC) use detectors to analyse the myriad of particles produced by collisions in the accelerator. These experiments are run by collaborations of scientists from institutes all over the world. Each experiment is distinct, and characterized by its detectors.

The biggest of these experiments, **ATLAS** (A Toroidal LHC Apparatus) and

CMS (Compact Muon Solenoid), use general-purpose detectors to investigate the largest range of physics possible. Having two independently designed detectors is vital for cross-confirmation of any new discoveries made. **ALICE** (A Large Ion Collider Experiment) and **LHCb** (Large Hadron Collider beauty) have detectors specialized for focussing on specific phenomena. These four detectors sit underground in huge caverns on the LHC ring [1].

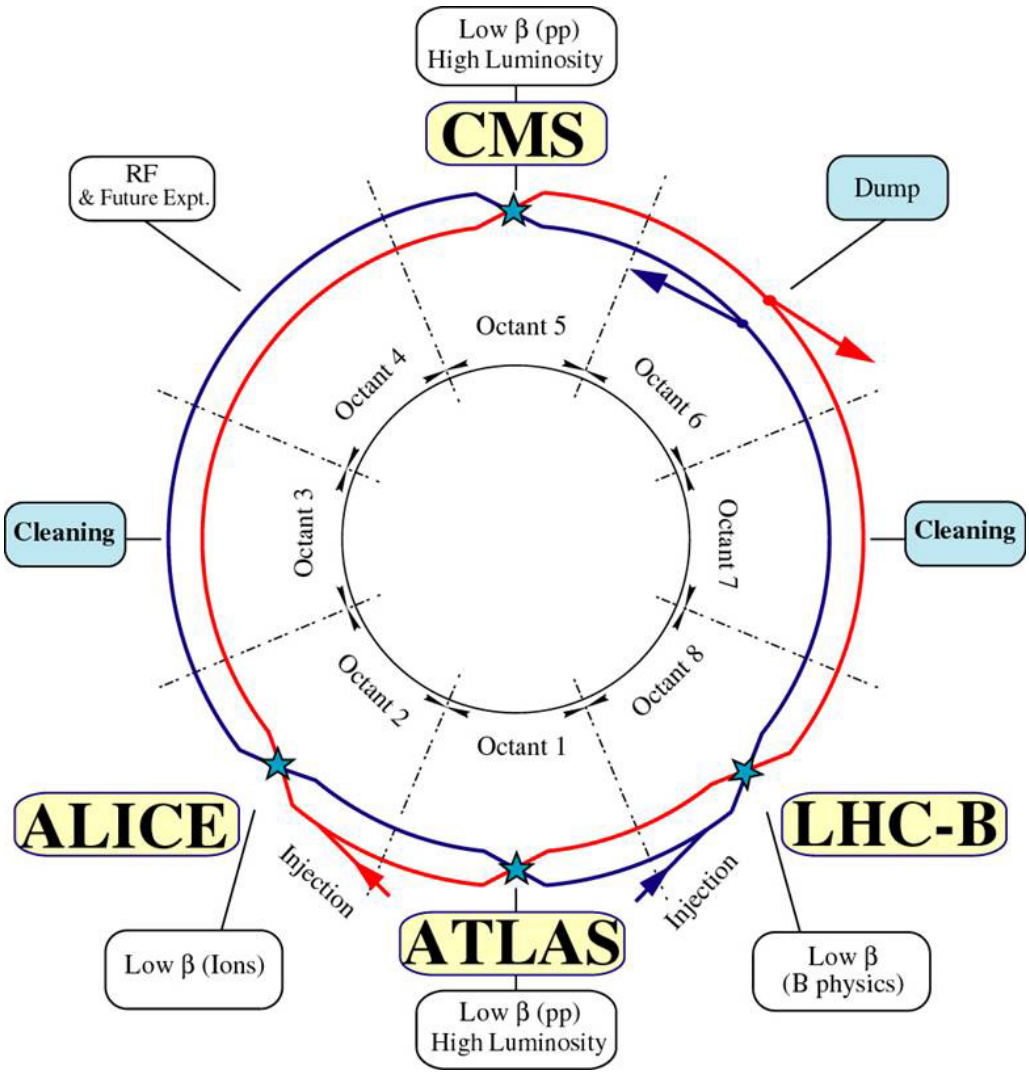

Figure 2.1: Overview schematic shows the four main experiments and the two ring structure of the LHC[1]

The smallest experiments on the LHC are **TOTEM** (Total elastic and diffractive cross-section measurement), **LHCf** (Large Hadron Collider forward) and **MoEDAL** (Monopole and Exotics Detector at the LHC).

2.2 The ATLAS detector

The ATLAS [2] is one of two general-purpose detectors at the Large Hadron Collider (LHC). At 46 m long, 25 m high and 25 m wide, the 7000-tonne ATLAS detector is the largest volume particle detector ever constructed. It sits in a cavern 100 m below ground near the main CERN site, close to the village of Meyrin in Switzerland. It investigates a wide range of physics, from the search for the Higgs boson to extra dimensions and particles that could make up dark matter.

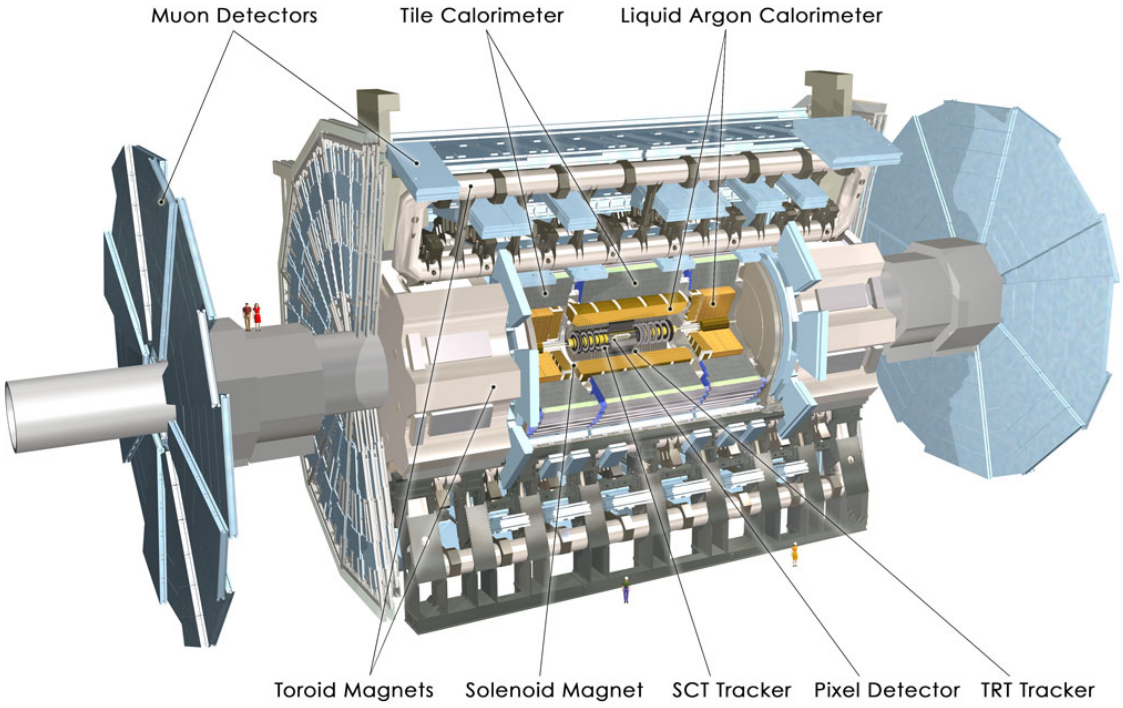

Figure 2.2: The ATLAS particle detector. [1]

It searching for new discoveries in the head-on collisions of protons of extraordinarily high energy. During protons collision new particles or resonances are created. In general, these produced particles quickly decay into two or more new particles, which in turn continue their path into the detector. These particles carry information about the proton interaction event which produced them, and the purpose of the ATLAS detector is to record as much information as possible about them. This is accomplished in the ATLAS by different detecting subsystems that identify particles and measure their momentum and energy (see Figure 2.2):

- **Inner Detector:** made from highly segmented silicon strips and Pixel detectors responsible for measuring the charged particles trajectories.
- **Hadron Calorimeter:** a device that measures the total energy of hadrons.
- **Electromagnetic calorimeter:** a device that measures the total energy of "electromagnetic showers" produced by electrons, positrons and photons.
- **Muon Detector:** a muon detection system consisting of precision drift tubes, resistive plate chambers, cathode strip chambers and thin gap chambers inside a toroidal magnetic field.

The detectors are divided into many sub-detectors because of the reason that each component tests for a special set of particle properties. Each particle type has its own "signature" in the detector. For example:

- **Charged particles**, like electrons and protons, are detected both in the tracking system and in the electromagnetic calorimeter.
- **Neutral particles**, like neutrons and photons, are not detectable in the tracking system. Photons are detected in the electromagnetic calorimeter, while neutrons are evidenced by the energy they deposit in the hadron calorimeter.
- **Muons** are detected in all components of the detector.
- **Neutrinos** are not seen by any of the detectors because they rarely interact with matter and their presence is inferred from the missing energy.

2.3 Inner detector

The layout of the Inner Detector [2] is shown in Figure 2.3. The Inner Detector comprises three complementary sub-detectors: the Pixel Detector, the Semiconductor Tracker (SCT) and the Transition Radiation Tracker (TRT). Relevant features are described briefly below; full details can be found in [2].

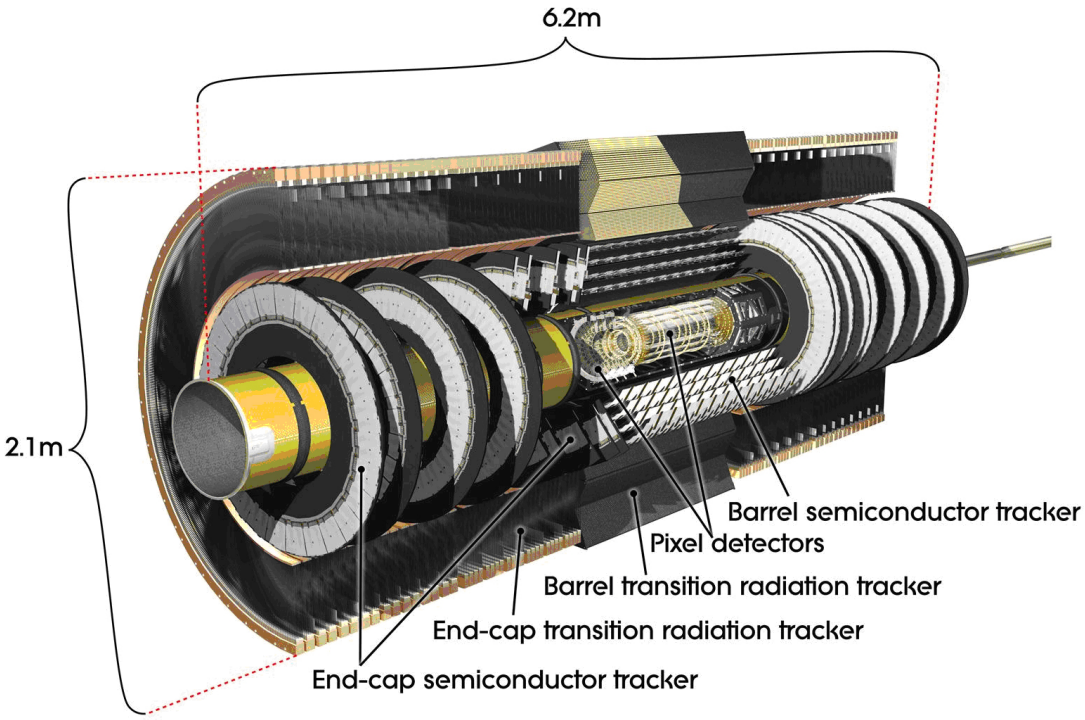

Figure 2.3: Cut-away image of the ATLAS Inner Detector.[3]

2.3.1 The Pixel detector

The Pixel Detector [2] sensitive elements cover radial distances between 50.5 mm and 122.5 mm. The detector consists of 1744 silicon pixel modules arranged in three concentric barrel layers and two endcaps of three disks each. It provides typically three measurement points for particles originating in the beam-interaction region. Each module covers an active area of 16.4 mm $\times$ 60.8 mm and contains 47 232 pixels, most of size 50 μm $\times$ 400 μm. With a total length of approximately 1.4m it typically detects three hits per traversing particles with pseudorapidity $|\eta| < 2.5$, with the transition between barrel and disk structures being at $|\eta| \approx 1.9$.

2.3.2 The Semiconductor Tracker (SCT)

The Semiconductor Tracer [2] (see Figure 2.4) sensitive elements span radial distances from 299 mm to 514 mm. The detector consists of 4088 modules of silicon-strip detectors arranged in four concentric barrels and two endcaps of nine disks

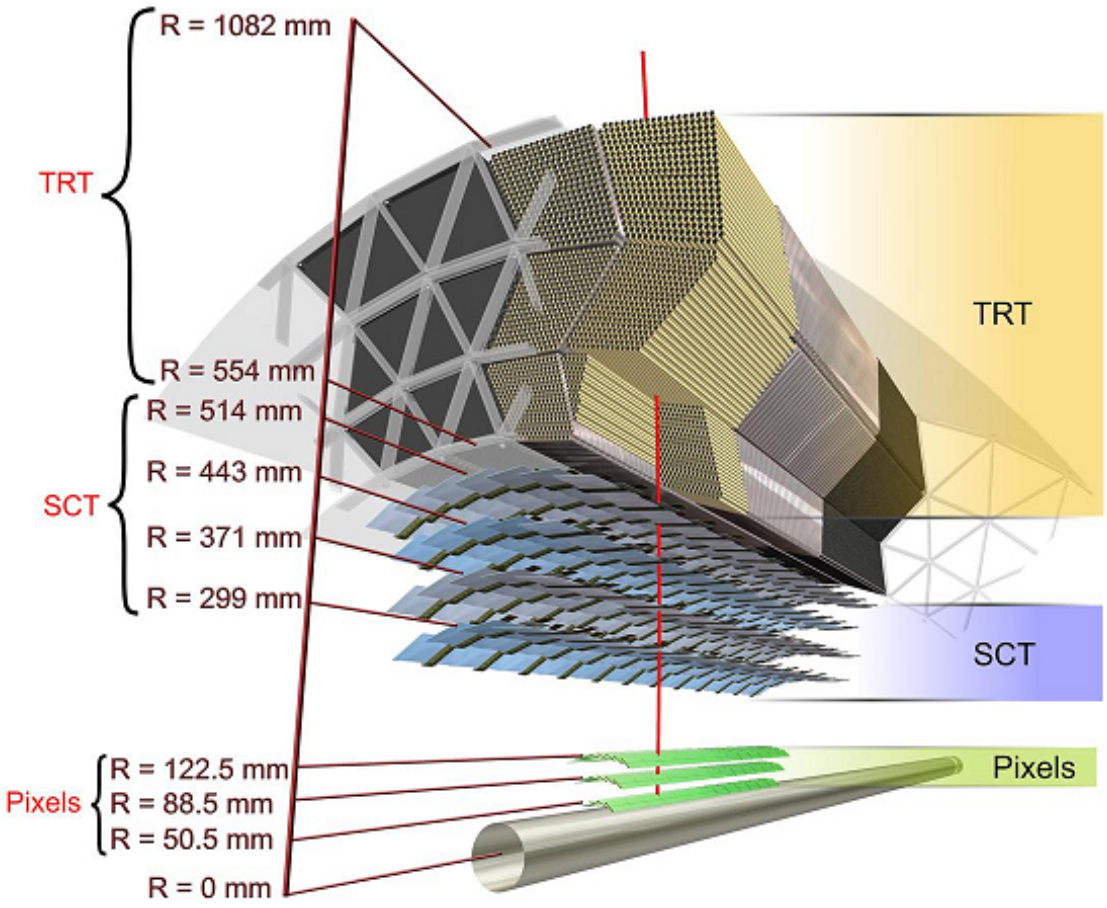

Figure 2.4: Layout of the ATLAS Inner Detector. [3]

each. It provides typically eight strip measurements (four space-points) for particles originating in the beam-interaction region. The strips in the barrel are approximately parallel to the solenoid field and beam axis, and have a constant pitch of 80 mm, while in the endcaps the strip direction is radial and of variable pitch. Most modules consist of four silicon-strip sensors; two sensors on each side are daisy-chained together to give 768 strips of approximately 12 cm in length. A second pair of identical sensors is glued back-to-back with the first pair at a stereo angle of 40 mrad to provide space points.

The end-cap modules are made of two or four wedge-shaped sensors of varying

size depending on their position on the end-cap rings. The strip pitch varies from 57 μm on the inner edge of the innermost sensors to 94 μm on the outer edge of the outermost sensors. The sensor pairs are mounted on a thermally highly conductive carbon base board that provides cooling. The SCT sensors are operated at -7^oC to prevent reverse annealing radiation damage.

2.3.3 The Transition Radiation Tracer (TRT)

The Transition Radiation Tracker [2] sensitive volume covers radial distances from 554 mm to 1082 mm. It is the outermost part of the Inner Detector. It provides charged-particle tracking based on the use of straw detectors, as well as electron identification through transition radiation measurements. Electron identification capability is added by employing Xenon gas to detect transition radiation photons created in a radiator between the straws.

The detector consists of a 144 cm long cylindrical barrel layer ranging from 56 to 108 cm in radius and two end-caps ranging from 84 to 271 cm in Z and 64 to 103 cm in radius. Both barrel and end-cap parts contain similar carbon-polyimide straw tubes of 4 mm in diameter which are equipped with a 30μm diameter gold-plated W-Re wire. The straws are filled with nonflammable gas mixture of 70% Xe, 27% CO_2 and 3% O_2. The straws are operated in proportional mode with the electrodes being on approximately 1530 V bias. The 52544 straws in the barrel form two modules embedded in polypropylene radiator foils in which transition radiation is produced. These modules are then formed into three rings to compose the entire barrel such that the straws are parallel to the Z-axis. The end-caps are composed of 160 planes of 122880 radially arranged straws of 37 cm length. The space between each pair of planes is filled with polypropylene radiator.

The TRT straw layout is designed so that charged particles with transverse momentum $p_T > 0.5$ GeV and with pseudorapidity $\eta < 2.0$ cross typically more than 30 straws.

2.4 Calorimetry

The calorimeters measure the energy of electrons, photons, isolated hadrons, and perhaps most importantly, jets. It is also deployed for the measurement of missing energy and the detection of low-p_T muons. A diagram of the ATLAS calorimetry is given in Figure 2.5 The overall pseudorapidity coverage is $|\eta| < 4.9$

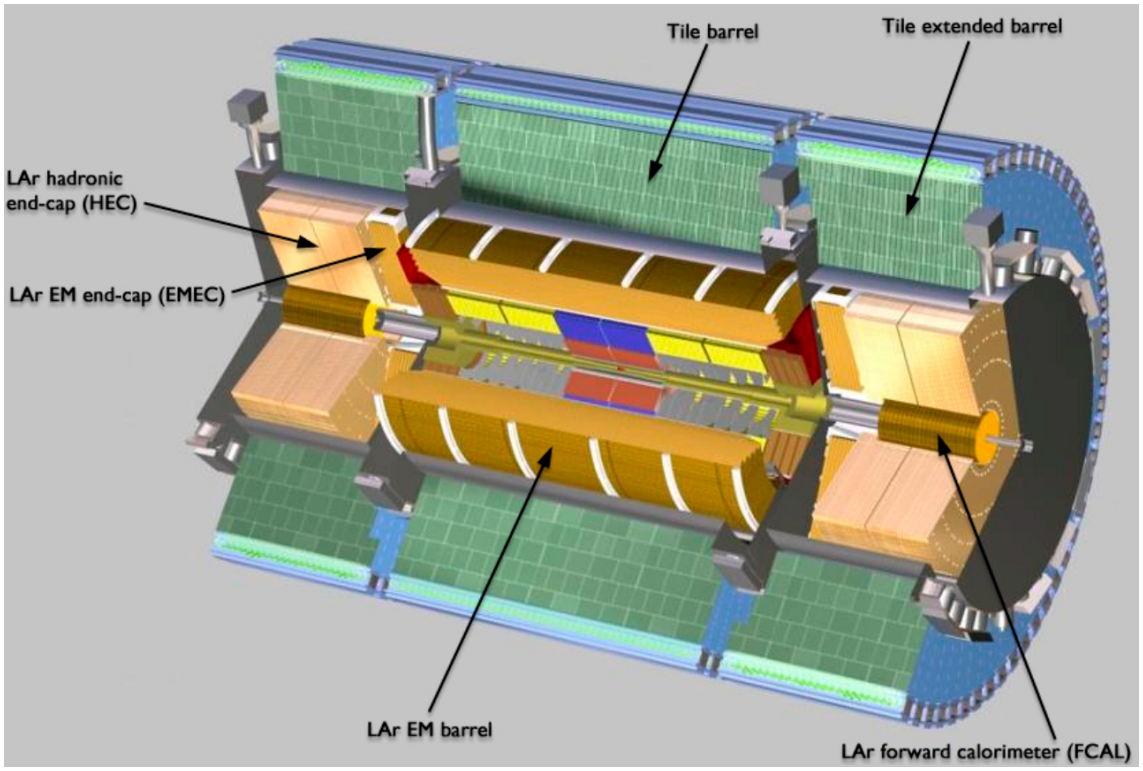

Figure 2.5: 3D schematic of the ATLAS calorimetry. [4]

There are two calorimeter systems - the **electromagnetic calorimeter**, for photons and electrons, and the **hadronic calorimeter**, for isolated hadrons and jets. Both systems are divided up into a cylindrical barrel and two end-caps for forward measurements. The calorimetry is located downstream of the inner detector and the central solenoid.

The ***electromagnetic calorimeter*** is a lead/liquid argon detector, with accordionshaped electrodes and absorber plates. The barrel provides coverage in the pseudorapidity region $|\eta| < 1.475$. The length of each half-barrel is 3.2 m and the inner and outer radii are 2.8 m and 4m respectively. It is in two pieces, with a 6 mm gap at z = 0. The barrel electromagnetic calorimeter shares the same cryostat

with the central solenoid. The end-cap E.M. calorimeters are in two discs, the inner disc covering $2.5 < |\eta| < 3.2$ and the outer wheel covering $1.375 < |\eta| < 2.5$.

The ***hadronic calorimeter*** uses the intrinsically radiation-hard liquid argon technology for higher pseudorapidities, where radiation levels will be higher, and plastic scintillator tiles embedded in iron absorbers for lower values ($|\eta| < 1.7$). The tile calorimeter is divided into one central barrel and two extended barrels. The inner and outer radii are 2.28 m and 4.25 m respectively. The scintillator tiles, 3 mm in thickness, are arranged radially in a periodic fashion, with a total iron thickness of 14 mm in one period. The emissions from each tile are read into two photomultipliers, one for each side, via fibre optics.

The end-caps cover the range $1.5 < |\eta| < 4.9$, where LAr calorimetry is used. They consist of inner and outer discs, the outer discs covering $|\eta|$ values below 3.2 and the inner discs dealing with values below 4.9. These inner discs are referred to as the Forward Calorimeter, and this must exist in a particularly challenging radiation environment.

Aside of the energy measurement role of the calorimetry, it should also act as a filter to remove all particles other than muons, such that readings from the muon spectrometer, located downstream of the hadronic calorimeter, are not polluted by hadrons. The hadronic calorimeter has a thickness of eleven radiation lengths at $\eta = 0$, which reduces punch-through of showers into the muon systems to a minimum.

2.5 The muon spectrometer

High p_T muons comprise the signatures of many interesting physics events, and the identification and measurement of the momentum of these particles is vital to the trigger system. These tasks fall to the **muon spectrometer**. Broadly speaking the muon system must perform two r^oles - the precise measurement of muon tracks (and hence momenta) and the provision of additional information for the trigger systems, such as bunch crossing identification and rapid momentum cut-off measurements.

The muon system is located in the outermost parts of the detector, downstream of the hadronic calorimetry. It is the only detection system in ATLAS that will be visible from the outside of the detector. Momentum measurement is facilitated

by the superconducting toroid magnets, where the barrel toroid provides field in the range $|\eta| < 1.0$ and the end-caps cover the range $1.4 < |\eta| < 2.7$. The region $1.0 < |\eta| < 1.4$ is covered by a combination of fields from both the barrel and the end-cap toroids.

In the barrel, the muon chambers are arranged in three cylindrical layers ("stations") whereas in the end-cap and transition region, the layers are positioned vertically. The technologies used in the detection elements differ depending on pseudorapidity and whether they are to be used for precise tracking or trigger measurements. Throughout most of the pseudorapidity range the detection elements used for tracking are **Monitored Drift Tubes** (MDTs). For high η and close to the interaction point, highly granular **Cathode Strip Chambers** (CSCs) are deployed. The trigger system, which covers the region $|\eta| < 2.4$, also uses two types of detector elements - **Resistive Plate Chambers** (RPCs) in the barrel and **Thin Gap Chambers** in the end-caps. The design and performance of these elements is covered in detail in [5].

2.6 ATLAS forward detectors

In addition to the ATLAS main detector which was just described, forward detectors are installed around the interaction point (IP). They are placed further from the IP to measure the forward energy flow to perform luminosity monitoring, luminosity absolute measurement, and other forward physics studies. Among these detectors will be ATLAS Forward Proton detectors.

2.6.1 ATLAS Forward Proton (AFP) project

The ATLAS Forward Proton (AFP) project plans to add a set of detectors to both sides of the ATLAS experiment at the LHC, which will allow to identify forward

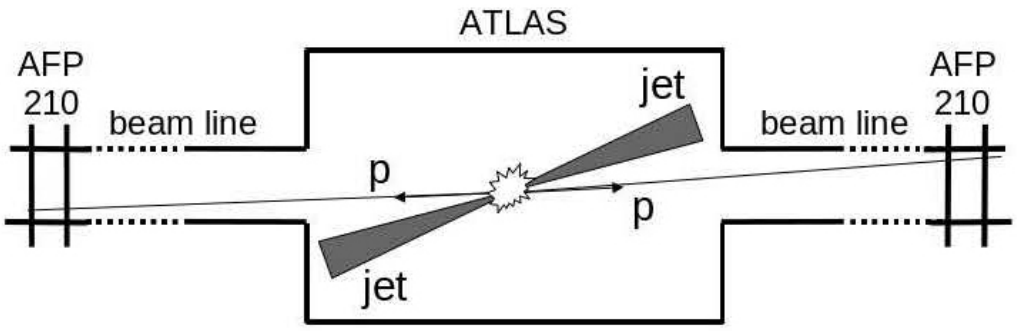

Figure 2.6: Schematic view of detection of forward protons produced at a very small angles by AFP detectors. [6]

protons produced at very small angles, of the order of microradians, and into the accelerator beampipe. Therefore, in order to detect the protons, detectors that are placed inside the machine beampipe are neccessary. Such measurements are challenging, but it has been shown at HERA, Tevatron and RHIC that they are possible. Although the ATLAS Experiment already has such detectors (the ALFA stations), their purpose is to measure the elastic scattering process and they can work only during special, very low luminosity LHC runs with a dedicated, high β^*, machine tune. The AFP is an upgrade project for the ATLAS experiment aiming to install additional detectors that will be able to detect forward protons during the normal LHC runs. The primary goal for the new detectors is to study the Central Exclusive Production, especially the exclusive WW production. A forward proton, which is scattered into the beampipe, propagates through the LHC magnetic system together with the proton beam. However, due to the energy loss in the interaction, its momentum is smaller than the nominal one. Therefore, in the magnetic fields of the LHC magnets its trajectory is bent more than the trajectory of the protons of the beam. The transverse distance between the beam and the forward proton increases with the distance from the IP, see Figure 2.7, and at some point the forward proton hits the beampipe. Before this happens, the proton is separated enough in the transverse scan from the beam to be tagged by the dedicated detectors.

The AFP project assumes installation of eight stations with such detectors around the ATLAS IP. The installation is planned in two phases:

1. **AFP220** – stations at 206 and 214 m (on both sides of the IP),

2. **AFP420** – stations at 416 and 424 m (on both sides of the IP).

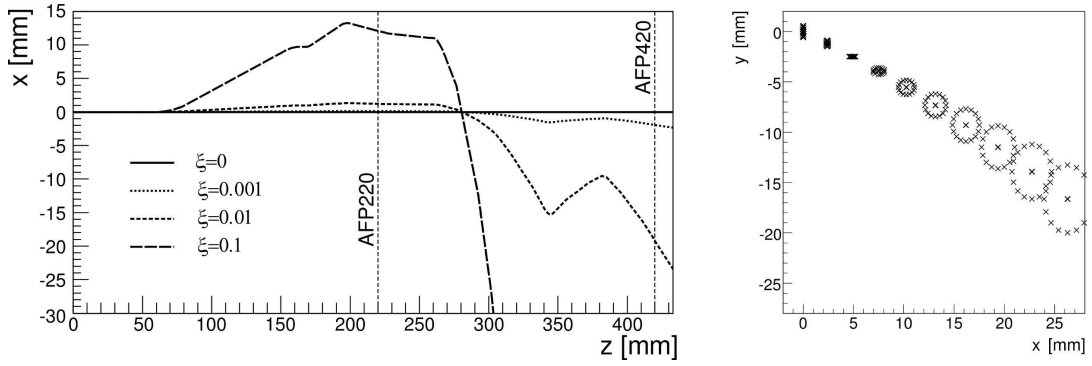

Figure 2.7: Left: Simulated horizontal trajectory of a 7 TeV proton and protons with tree different values of reduces energy loss. **Right:** The position of scattered protons in the AFP220. Moving from left to right, different ellipses correspond to increasing values of ξ, the centers of ellipses correspond to $t = 0.0\ GeV^2$, while the ellipses correspond to $t = 0.5\ GeV^2$. [6]

The first phase of the installation (AFP220) is planned for the long LHC shutdown starting in 2012. These detectors can be used for the studies of exclusive production of jets and anomalous couplings. The second phase (AFP420) is more complicated from the technical point of view, because the 420 m area is already the LHC cold region and in order to install the detectors one needs to interfere with the machine liquid helium system.

The AFP420 stations are needed for the Higgs mass studies, but are not necessary for the anomalous coupling study. Therefore, the second phase of the AFP project will possibly be performed only if the SM Higgs is discovered and the uncertainty for its production in the exclusive mode is more constrained.

The second phase could be also considered in the case of supersymmetric particles discovery. Figure 2.8 shows the scheme of the long straight section of the ATLAS forward region with marked positions of proposed AFP220 stations. The AFP220 will consist of two stations:

1. **AFP1** – at 206 m instrumented with the 3D silicon tracking detector,

2. **AFP2** – at 214 m instrumented with the 3D silicon tracking detector and the time of flight detector.

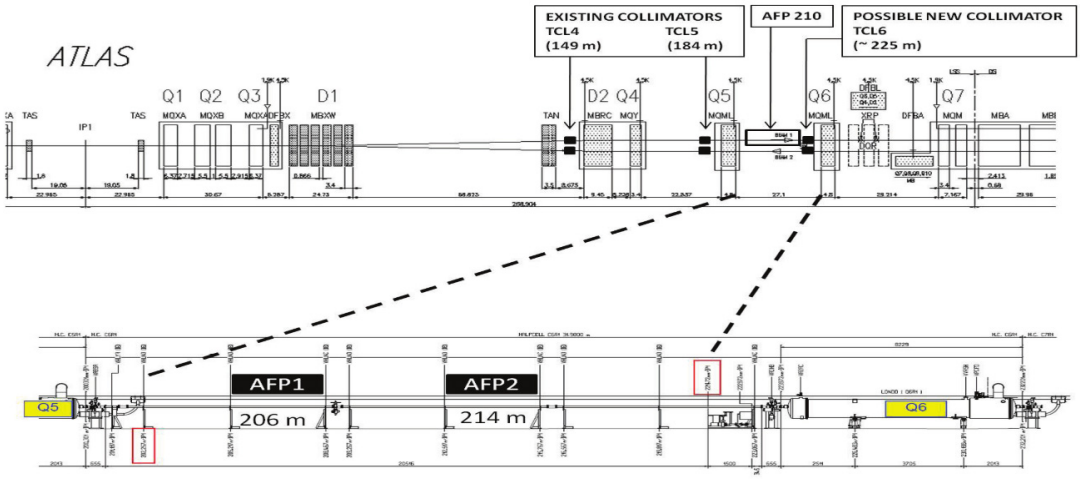

Figure 2.8: Schema of the long straight section of the ATLAS forward region with marked positions of the AFP stations at 206 and 214 m. D1 and D2 are dipole magnets and Q1–Q7 are quadrupole magnets. [7]

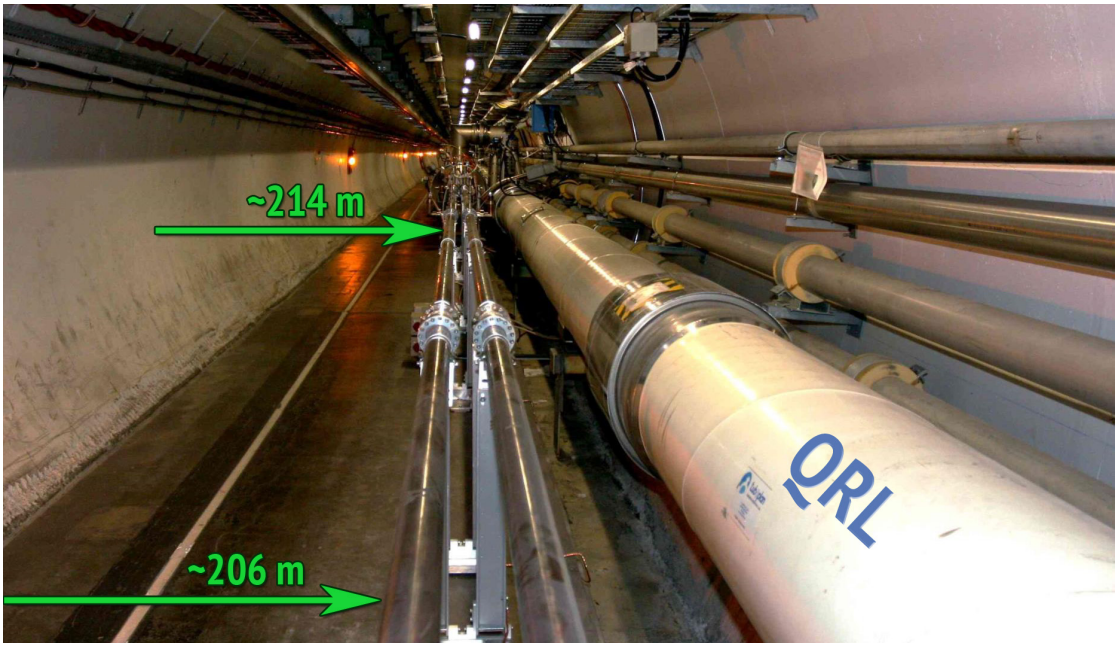

Figure 2.9: AFP220 location. Photo. [8]

Hamburg beam pipe

To perform the measurement of forward protons, detectors that are placed inside the accelerator beampipe are required. The smaller the distance between the active detector area and the beam, the better the acceptance that can be obtained. However, one must realise that in the beginning of most runs the beam is “hot”,

which means that it can be unstable. In order to perform the measurements the detectors need to be movable – it must be possible to adjust their position (i.e. their transverse distance to the beam) appropriately to the beam conditions. The AFP project assumes the use of the Hamburg movable beampipe mechanism to adjust the horizontal position of the detectors, see Figure 2.10.

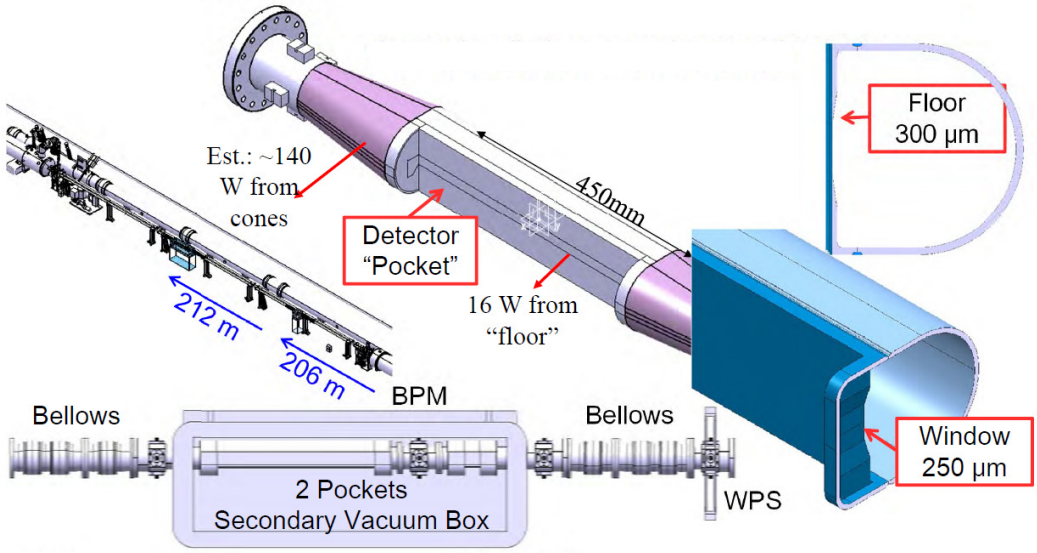

Figure 2.10: Design of the Hamburg beam pipe with marked regions of the thin window and the floor. [7]

The beam pipe wall is very thin (less than 300 μm) in the area of the so-called floor and thin window to minimize the interaction of beam particles with the wall material and the distance of the detectors to the beam. The Hamburg beam pipe will be used in two length variations — short (with 100 mm long detector pocket) for tracking detectors and long (700 mm long pocket) for QUARTIC timing detectors.

The Hamburg beam pipe will be installed on a moving table to allow horizontal movement of detectors (see Figure 2.11). To ensure the quality of the vacuum in detectors, the whole assembly of the Hamburg beam pipe and the detectors will be placed in a secondary vacuum box.

Tracking Detectors

For the measurement of the proton position the required resolution is the 10 μm in horizontal and 30 μm in the vertical direction. Additional **important require-**

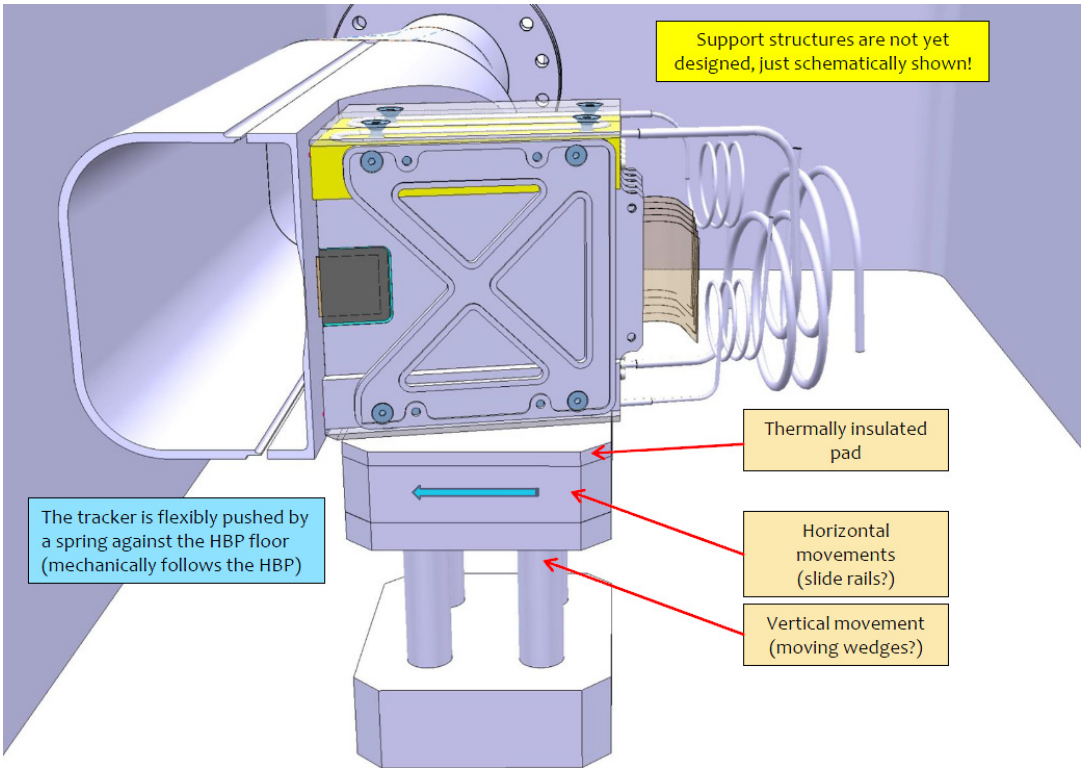

Figure 2.11: Tracker integrated in the Hamburg beam pipe. [9]

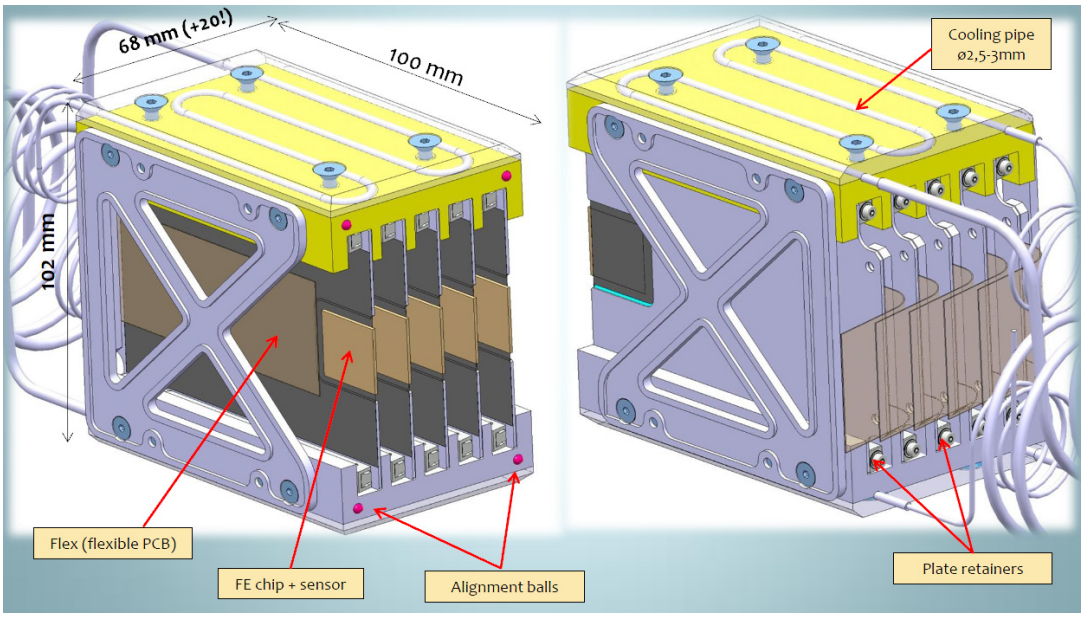

Figure 2.12: The AFP tracker mechanics.[9]

ments for the detectors are: high efficiency, small dead space at the edge of the sensors (active edge) and sufficient radiation hardness. A 3D silicon tracking detectors (more details about 3D silicon sensors can be found in Chapter 4) fulfilling

these requirements will be placed in each AFP station. Such detector will consist of five layers of active detectors that will together give the required resolution (Figure 2.12).

Time of Flight Detectors

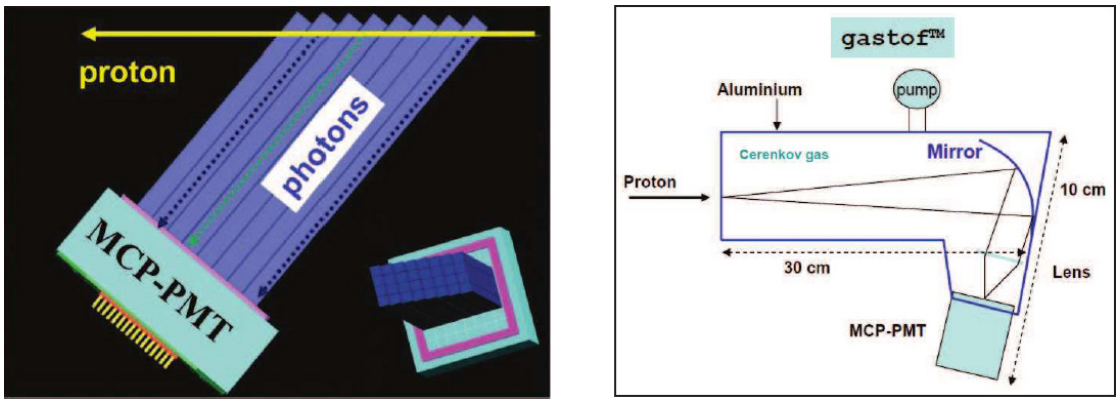

Figure 2.13: Left: A schematic side view of the proposed QUARTIC time-of-flight counter, which shows Cherenkov photons being emitted and channeled to the MCP-PMT as the proton traverses the eight fused silica bars in one row. The inset shows a rotated view with all four rows visible. **Right:** A schematic view of the proposed GASTOF time-of-flight counter.[7]

At the LHC one needs to take pile-up into the account. Not only will the bunch crossings occur every 25 ns, but also in each of them many independent pp interactions will occur. For studies of the Central Exclusive Production it must be possible to tell if both protons observed in the AFP detectors come from the same interaction (the same vertex) or it is just a random coincidence of two intact protons coming from two different, independent pp collisions. For this purpose additional detectors are needed – fast timing detectors with resolution of a few picoseconds. With such detectors it is possible to measure the proton time of flight from the vertex to the AFP station so precisely that it will be possible to reconstruct the longitudinal position of the interaction vertex with resolution of a few millimeters. Such measurement performed for both protons will help to distinguish the signal from the pile-up background.

Two different designs of timing detectors are considered. The first one, QUARTIC (see Figure 2.13 left), consists of a matrix of quartz bars. A proton traversing

the detector creates Cherenkov light that propagates along the bars to the photomultiplier. In the second detector, GASTOF, a gas is used as the active material and the created Cherenkov light is focused by a mirror and then detected by a photomultiplier (see Figure 2.13 right).

Kinematics of a forward proton is often described by means of the reduced energy loss ξ:

$$\xi = \frac{\Delta E}{E_0} = \frac{E_0 - E}{E_0}, \tag{2.1}$$

where E_0 is the nominal energy of the beam, E is the energy of the proton after the interaction and ΔE is the energy that proton lost in the process. For the Central Exclusive Production there is a simple approximate relation between the reduced energy losses of both protons (ξ_1 and ξ_2) and the mass M of the centrally produced particle/system (missing mass):

$$M^2 = s \cdot \xi_1 \cdot \xi_2, \tag{2.2}$$

where $s = (2E_0)^2$ is the centre of mass energy squared.

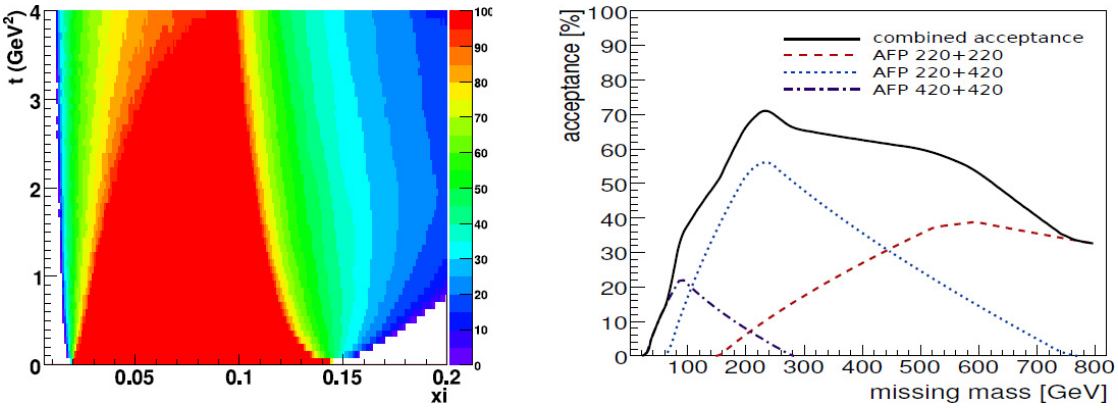

Figure 2.14: Left: Acceptance of the AFP220 stations on beam 1 as a function of ξ and $t \approx p_T^2$. **Right:** Acceptance of the AFP detectors as a function of the missing mass. [6]

Both sets of detector stations (AFP220 and AFP420) are needed to cover a wide range of ξ. The AFP220 stations can detect protons with ξ between 0.02 and 0.2, whereas the AFP420 stations accept $0.002 < \xi < 0.02$. The lower endpoints of these intervals depend on the distance between the detector and the beam (the smaller the distance, the smaller the minimal ξ). Figure 2.14 (left) shows the acceptance of the AFP220. For the Central Exclusive Production, the acceptances of both protons

can be converted into the acceptance as a function of the centrally produced mass, see Figure 2.14 (right). Three different signatures are considered in this plot:

1. AFP220+AFP220 – both protons are detected by the AFP220 stations.
2. AFP420+AFP420 – both protons are detected by the AFP420 stations.
3. AFP220+AFP420 – one proton is detected by the AFP220 station and the second one by the AFP420 station.

Chapter 3

Physics case for the AFP project

3.1 Introduction

In the high energy pp collisions at the LHC, main detector acceptance is in the central rapidity region, i.e. where the most of the particles are produced and where the most of the high p_T signal of new physics is expected.

Forward physics is devoted to studies of high rapidity regions and includes many interesting physics topics including the elastic scattering, diffraction, low-x QCD and Central Exclusive Production, and photon-photon interaction, the last two being the main motivation for the AFP project.

3.2 Central Exclusive Production

Central Exclusive Production (CEP) is class of processes in which the two interacting protons are not destroyed during the interaction but survive into the final state (intact protons, forward protons). Such situation takes place for example during elastic scattering, but can happen also in quasi-elastic processes when, apart from the two protons, there is an additional particle (or particles) in the final state.

This is a very rare situation and can occurs when the protons interact coherently

via the emission of a color singlet object. Such interaction can be of an electromagnetic or a strong nature, occurring via a photon or Pomeron exchange, respectively. In hard processes, the Pomeron exchange is usually modelled, at the lowest order, by an exchange of a colorless two-gluon system. Feynman diagrams for two important examples are presented in Figure 3.1 – exclusive production of jets (left) and the Higgs boson (right). One can notice a similar interaction structure: two gluons are emitted from each proton, one of the gluons is involved in the hard subprocess ($gg \to gg$ or $gg \to H$), the second one screens the process. Since no color is exchanged between the protons and the central state (jets or Higgs), it is possible that the protons stay intact after the interaction. It is important to point out that in the Central Exclusive Production, contrary to the Double Pomeron Exchange processes, there are no Pomeron remnants in the final state.

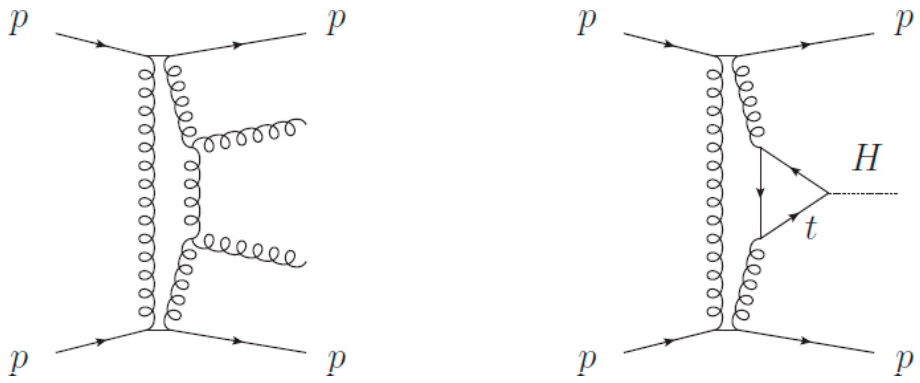

Figure 3.1: Feynman diagrams of exclusive jets (left) and Higgs (right) production.

The exclusive jet production has already been studied at the Tevatron [10] and there is a possibility for observing the exclusive Higgs at the LHC. This would have several advantages over the "standard" searches. First of all, the exclusive $\bar{b}b$ jets production (background to exclusive $H \to \bar{b}b$) is suppressed by the $J_z = 0$ selection rule. Secondly, for such a process it is possible to detect all particles in the final state, provided the forward protons are detected. In such a way the kinematics of the event is fully constrained, which leads to a good resolution for the Higgs mass measurement in a wide range of masses [11]. Thirdly, observing the Higgs in the exclusive production mode indicates strongly that it is a 0^{++} particle, since the amplitudes for other spin states are much smaller. The drawback of this approach

for the Standard Model (SM) Higgs is a very small production cross section, which is predicted (with very large uncertainty) to be of the order of a femtobarn. However, in supersymetry (SUSY) scenarios the cross section can be much larger.

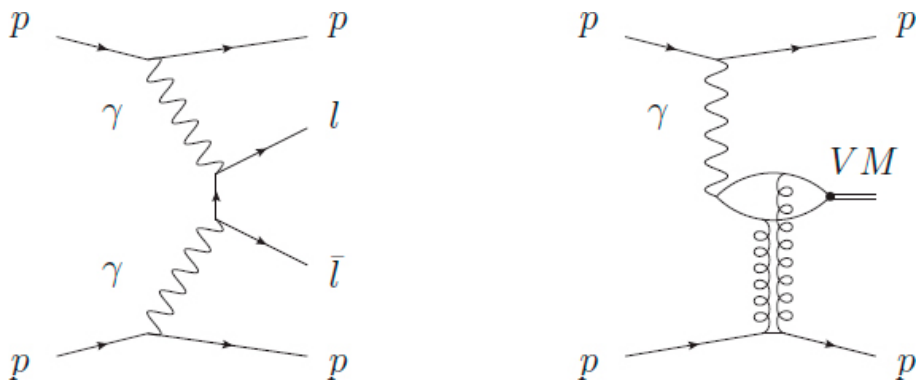

Figure 3.2: Feynman diagrams of diphoton exchange (left) and exclusive photoproduction (right) processes.

As mentioned before the exclusive production can be not only a strong interaction, but also an electromagnetic one. A Feynman diagram for an example of such a process is shown in Figure 3.2 (left). One can see that the photons which are emitted from the protons, interact with each other and produce a lepton pair. This kind of process is called a photon-photon interaction and the same mechanism can lead to a production of pairs of W bosons, sparticles, etc. Since these are the QED processes, they are well understood and the prediction for cross sections have very small uncertainty. Therefore, they can be used for a precise luminosity determination at the LHC [12]. Also, similarly to the exclusive Higgs case, the detection of the outgoing protons can give a precise determination of the central system mass, which can be used for SUSY studies [13].

There exists also a third possibility of the exclusive process. It is the exclusive photoproduction and it combines the electromagnetic and strong interactions. Here, one of the protons emits a photon that interacts with the Pomeron emitted by the second proton, see Figure 3.2 (right). The result is a vector meson and two intact protons in the final state.

3.3 Anomalous Gauge Bosons Couplings

A particularly interesting exclusive process that could be studied at the LHC is the production of W boson pairs. A complete overview of this process can be found in [14, 15], only the main points are outlined in this chapter. As mentioned above, a WW pair can be produced in a photon-photon process, see Fig. 3.3 (left). The cross section is calculated as a convolution of the photon-photon luminosity $L_{\gamma\gamma}$ and the subprocess cross section $\hat{\sigma}_{\gamma\gamma\to WW}$:

$$\sigma_{pp\to pW^+W^-p} = \int L_{\gamma\gamma}\hat{\sigma}_{\gamma\gamma\to WW} \tag{3.1}$$

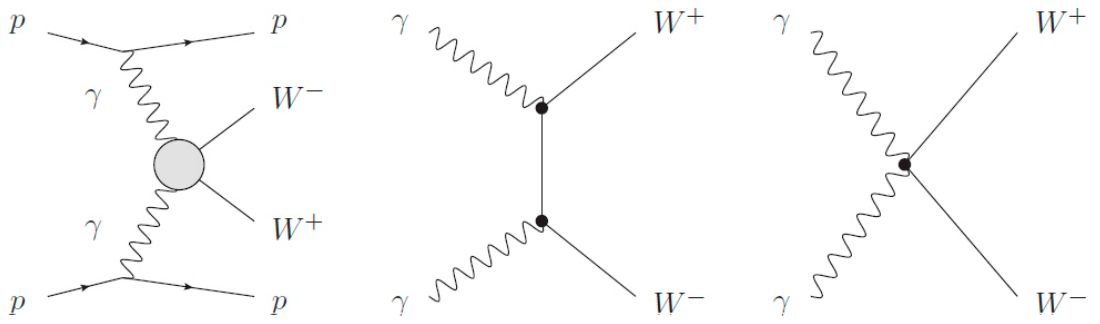

Figure 3.3: The Feynman diagram of an exclusive W^+W^- production in photon-photon interaction (left) and diagrams contributing to the $\gamma\gamma \to W^+W^-$ subprocess via triple γWW (centre) and quartic $\gamma\gamma WW$ (right) SM couplings.

Measurements of this process will allow to probe the SM quartic $\gamma\gamma WW$ couplings, which can give an insight into the electroweak symmetry breaking mechanism. Also, it is expected in the Beyond Standard Model (BSM) theories (especially in Higgsless and extra-dimension models) that the cross section for exclusive WW production is larger than in the SM.

Such BSM effects can be described in terms of anomalous couplings of the gauge bosons. This is done by adding into the SM Lagrangian new (anomalous) terms that are responsible for the modified interactions. The cross section for the WW production in the photon-photon channel rise very quickly with the anomalous couplings values. With the AFP detectors one can constrain the values of the couplings by four orders of magnitude and reach the values predicted by Higgsless and extra-dimension models.

Chapter 4

Silicon detectors

Particle detection in silicon detectors is based on electron/hole (e/h) pair creation which happens when particles crossing the detector lose sufficient energy. This energy loss is due to the interaction of the travessing particle with the silicon.

4.1 Interaction of radiation with a matter

It is necessary to understand the interaction of radiation with matter, in order to study how particle detection is done. Because of the energy loss of particles depends on the particle mass, heavy charged particles and light charged particles will be discussed separately.

4.1.1 Heavy charged particles

When heavy particles (i.e. particles with mass much larger than the electron mass) passing through a material they lose energy mainly due to ionisation and excitation. The stopping power for the heavy charged particles can be described with the *Bethe-Bloch* equation:

$$-\langle\frac{dE}{dx}\rangle = 2\pi N_A r_e^2 m_e c^2 \rho \cdot \frac{Z}{A} \cdot \frac{z^2}{\beta^2} \cdot (\ln \frac{2m_e\gamma^2 v^2 T_{max}}{\Phi^2} - 2\beta^2 - \delta - 2\frac{C}{Z}), \qquad (4.1)$$

where c is the speed of light, $\beta = \frac{v}{c}$, $\gamma = \frac{1}{\sqrt{1-\beta^2}}$, m_e the electron mass, e the electron charge, N_A is the Avogadro number, ρ the density of the material, m_e the

electron mass, e the electron charge, z the charge of the traversing particle, Z the atomic number of the material, A its atomic weight, Φ the average ionization energy of the material, δ is a correction factor, C a shell correction and T_{max} the maximum energy for an incident particle of mass:

$$T_{max} = \frac{2m_e c^2 \beta^2 \gamma^2}{1 + \frac{m_e}{M} \cdot \sqrt{1 + \beta^2\gamma^2} + \frac{m_e^2}{M}}. \tag{4.2}$$

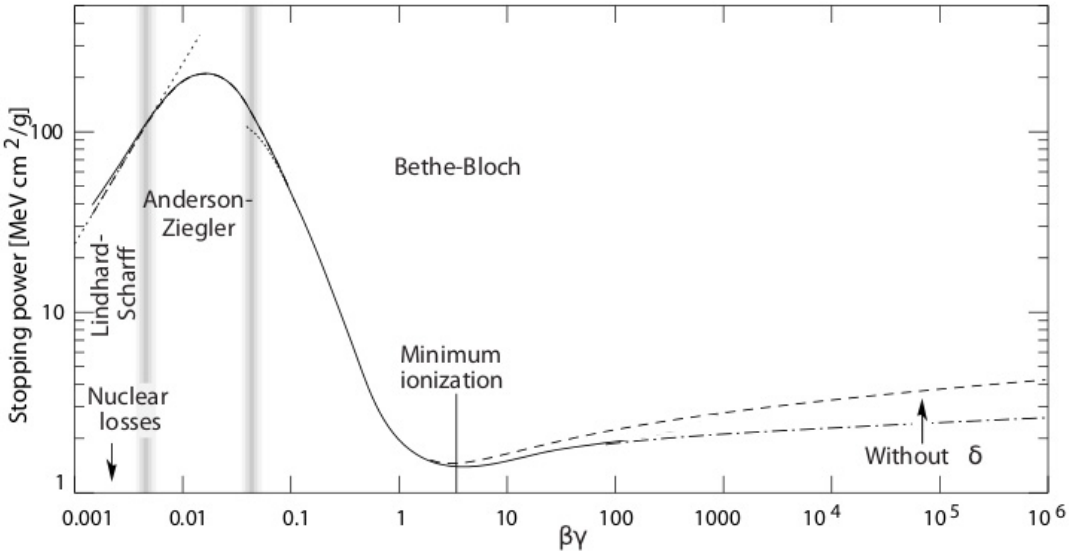

Figure 4.1: Enegy loss of a muon in copper, as a function of $\beta\gamma$ [16].

In Figure 4.1 one can see the energy loss of a muon in copper, as a function of $\beta\gamma$. Notice that $\beta\gamma$ increases when the velocity is increased and therefore, the kinetic energy. At $\beta\gamma < 0.1$ the Bethe-Bloch equation does not work, as other energy loss mechanisms become important. Above that point the $\frac{1}{\beta^2}$ term dominates until the energy loss reaches minimum value around $\beta\gamma \approx 3$ and then rises proportionally to $\ln \beta\gamma$. This minimum value is almost same for any material, as it decreases slightly when increasing the atomic number of the material. A minimum ionizing particle (MIP) is defined as a particle whose energy loss ratio is close to the minimum. In practical cases, most of the charged particles with hight momentum can be considered MIPs.

For example for silicon, the minimum ionization energy loss, $\langle \frac{dE}{dx} \rangle = 1.5\ MeVcm^2/g$.

4.1.2 Light charged particles

The energy loss for the light charged particles is dominated by the radiative loss (bremsstrahlung) and not by ionisation.

In the bremsstrahlung process, photons are radiated by a particle due to the acceleration in electromagnetic fields. The radiative energy loss is proportional to the incident energy and depends on the material crossed:

$$(\frac{dE}{dx})_{brem} = -\frac{\rho E}{X_0}, \tag{4.3}$$

where ρ is the density of the material and X_0 is the radiation length, i.e. the distance at which the energy has decreased by a factor e due to the radiative loss.

4.1.3 Photon interactions with matter

Photons passing through a material are absorbed, so the number of photons penetrating a depth x is described by:

$$\frac{dN}{dx} = -N\frac{\rho N_A \sigma}{A}, \tag{4.4}$$

where N_A is Avogadro's constant, ρ is the density of the material, A is its atomic mass and σ is the absorption cross section, which depends on the absorption mechanism as:

$$\sigma_{tot} = \sum_{abs.mech} \sigma_i. \tag{4.5}$$

The electromagnetic radiation can interact with matter mainly by three processes contributing to the total cross section:

- **Photoelectric effect:** Photons are absorbed by electrons of the material when the energy of the photon energy exceeds the ionization potential (Φ), emitting the electron with an energy:

$$E = h\omega - \Phi, \tag{4.6}$$

$h\omega$ being the incident photon energy. Then, photoelectric effect creates free charge carriers in the silicon detector. As Φ depends on the atomic charge Z, the cross section in photoelectric effect also depends strongly on Z.

- **Compton scattering:** Photons collide with free electrons of the material with an incident angle θ, lowering the photon's frequency ω:

$$\frac{1}{\omega_f} - \frac{1}{\omega_0} = \frac{h}{m_e c^2}(1 - \cos\theta); \tag{4.7}$$

- **Pair production:** Photons with energy higher than 1.022 MeV can create e^+/e^- pairs, which can emit photons by bremsstrahlung.

4.2 Semiconductor physics

Semiconductor detectors, as their name implies, are based on crystalline semiconductor materials, most notably silicon and germanium. Particle detection in silicon detectors is based on properties of semiconductor materials.

In this section, it will briefly review the basic properties of semiconductor materials and those electrical characteristics which are important for their use as radiation detectors.

Electrons in solids are grouped in two energy bands, the valence energy band and the conduction energy band (where they can move freely) separated (or not) by the forbidden levels of energy which can not be occupied. The electrons that contribute to the electrical conductivity are the ones with enough energy to reach the conduction energy band. The main difference between conductor, semiconductor and insulator materials is the size of their energy gap (ϵ_g), defined as:

$$\epsilon_g = \epsilon_c - \epsilon_v, \tag{4.8}$$

where ϵ_c is the lowest energy level of the conductor band and ϵ_v the largest energy level of the valence band. Then for $\epsilon_g = 0$ eV it is *Conductor*, for $0 < \epsilon_g < 2.5$ eV it is *Semiconductor* and for $\epsilon_g > 2.5$ eV it is *Insulator*.

All electrons in the semiconductor at $T = 0$ K are placed at the valence band orbitals, leaving the conduction band empty and by increasing the temperature, conduction bands start to be occupied by electrons which leave holes that contribute to the electrical conduction as particles with positive charge. Then there is a temperature dependence with the charge carrier particles concentration [17]:

$$n_i = (n_c n_v)^{1/2} \cdot e^{-\frac{\epsilon_g}{2k_B T}}, \tag{4.9}$$

where k_B is the Bolztmann constant, and $n_{c/v}$ are the effective density of states of the conduction/valence band:

$$n_{c/v} = 2\left(\frac{m_e k_B T}{2\pi h^2}\right)^{3/2}, \tag{4.10}$$

where m_e is the electron mass and h the reduced Planck constant. For silicon, the energy gap is about 1.12 eV, but the energy needed to generate an electron/hole pair is 3.61 eV because energy is absorbed also into phonons. A MIP creates around 80 e/h pairs per μm. At room temperature ($k_B T \approx 1/40$ eV), from Eq. 4.9 for a pure silicon semiconductor, n_i is about 10^{10} e^-/cm^{-3}. That is, for a surface device of about 1 cm^2, a total concentration of the order of 10^6 $e^-/\mu m$, many orders of magnitude greater than the e/h pair creation density per μm. To decrease the number of free carriers, the semiconductors are doped, and a depletion zone generated from a pn-junction.

Semiconductors and doping

The number of electrons is equal than the number of holes (i.e. a pure semiconductor), but semiconductors in devices have impurities added to increase the concentration of either conduction electrons (n-type) or holes (p-type). This process is known as doping. Doping is done by adding elements of the V. group of the periodic table such as phosphorus (for n-type) with an extra valence electron (donor) or III. group such as boron (for p-type) with one less valence electron (acceptor).

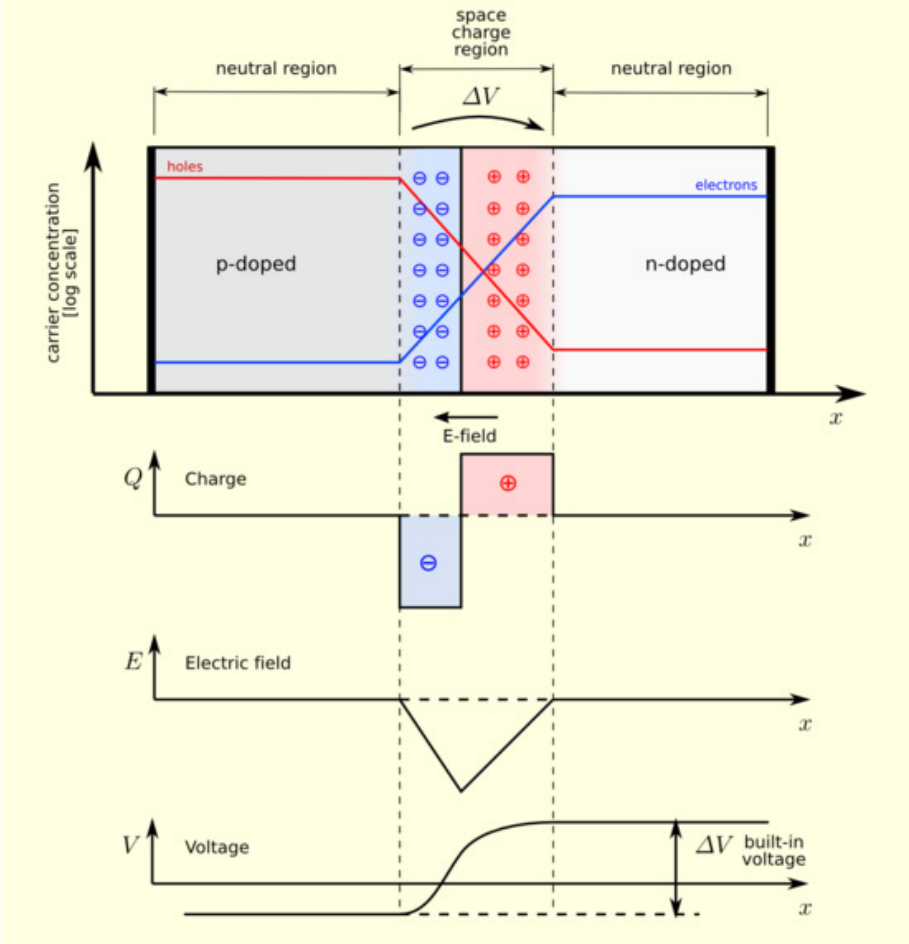

Figure 4.2: Charge carrier distribution, charge, electric field and voltage of a reverse biased abrupt pn-junction [16]

P-N junction

$$\rho = \begin{cases} -eN_A & -x_p < x < 0 \\ eD & 0 < x < x_n \end{cases} \tag{4.11}$$

Semiconductor (Si, Ge) in pixel devices are based on the formation of a p-n junction (Figure 4.2). The number of donors predominant on one side of the junction at a distance x_n and the number of acceptors on the other side at a distance x_p. Then, the charge distribution is described by Equation 4.11, where $N_{A/D}$ is the number of acceptors/donors. P-N junctions have intrinsic voltage V_{dep} without applying external voltage that can be found by integrating the expression:

$$\frac{dE}{dx} = \frac{1}{\epsilon}\rho(x), \tag{4.12}$$

therefore:

$$V_{dep} = \frac{e}{2\epsilon}(N_A x_p^2 + N_D x_n^2), \tag{4.13}$$

by neutrality condition:

$$N_A x_p = N_D x_n. \tag{4.14}$$

The distance at which the electric field is extended in the device is:

$$d = x_n + x_p = \sqrt{\frac{2\epsilon}{e} \cdot \frac{N_A + N_D}{N_A \cdot N_D} \cdot V_{dep}}, \tag{4.15}$$

it is named the depletion zone. Along this distance, the concentration of the free charge carriers lowers, decreasing the noise in the charge collection and allowing the charge generated by traversing particles to be collected. Normally, one side is much more doped than the other. Therefore, the contribution of the greater doped charge carriers can be neglected in the depletion width:

$$d = \sqrt{\frac{2\epsilon}{N_{D/A}} \cdot V_{dep}}. \tag{4.16}$$

4.3 Particle detection principles

A simple configuration of the semiconductor detector made by an absorbing medium, the semiconductor in PN junction configuration, with two highly doped p^+ and n^+ electrodes on the opposite side (see Figure 4.3). The electrodes are themselves connected to an external reverse bias supply, which creates the electric field in the PN junction and the depleted zone empty of free charges.

When a particle passes through the material and generates charged carriers this electric field makes the charges drift to the respective electrodes, holes to p^+ and electrons to n^+, producing the signal.

The full depletion voltage V_{depl} is the voltage needed to extend the depletion zone over the whole thickness d of the substrate:

$$V_{depl} = \frac{eN_D d^2}{2\epsilon_0 \epsilon_{Si}}, \tag{4.17}$$

and depends on the substrate thickness and the substrate doping concentration N_D

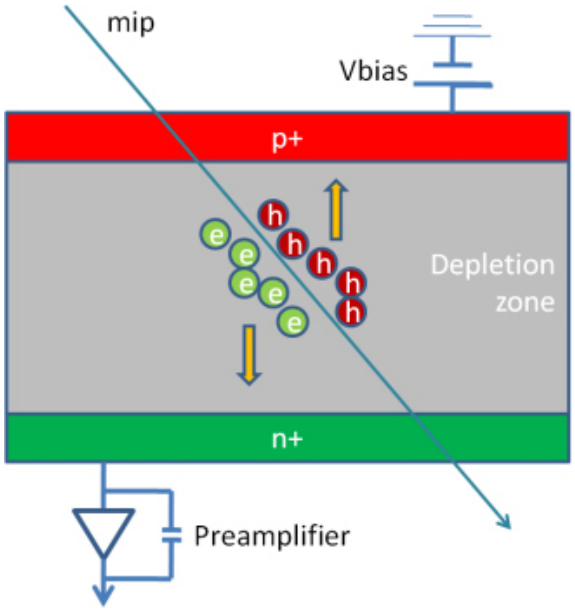

Figure 4.3: Example of silicon detector geometry [18]

4.4 Different types of silicon detectors

Silicon detectors can be obtained with different electrode shapes or different doping configurations, according to the performance, efficiency and resolution wanted. Thus one can differentiate mainly between two types of sensor: *strip detectors* and *pixel detectors* which can be also classiffied as *planar* and *3D pixel* detectors.

A **strip detector**, is obtained by creating one electrode segmented in thin parallel strips, and this is usually called a "single sided microstrip detector". The single sided strip detector has this pattern in one of its sides (n^+ or p^+), but only gives one dimensional information, so it is needed implement the same pattern perpendicularly at the other side. But even with both n+ and p+ sides with strip perpendicular

patterns, when two or more particles hit the same strip there are ambiguities in the readout.

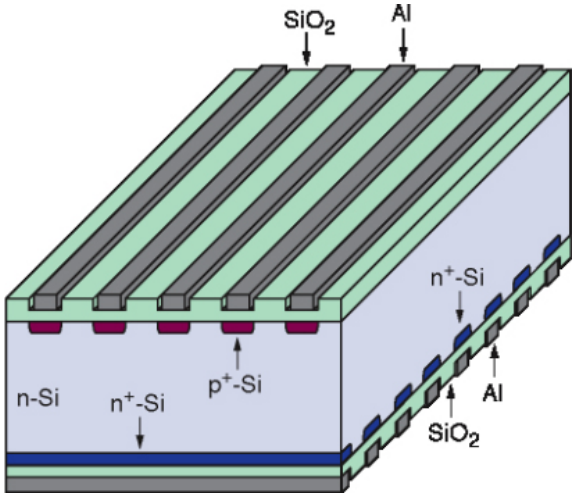

Figure 4.4: Layout of a double-sided microstrip detector [19]

Pixel detector solves the ambiguity problem of the strip detector. They measure both spatial coordinates on the same side of the sensor, and segmentation is therefore necessary only on one side of the sensor.

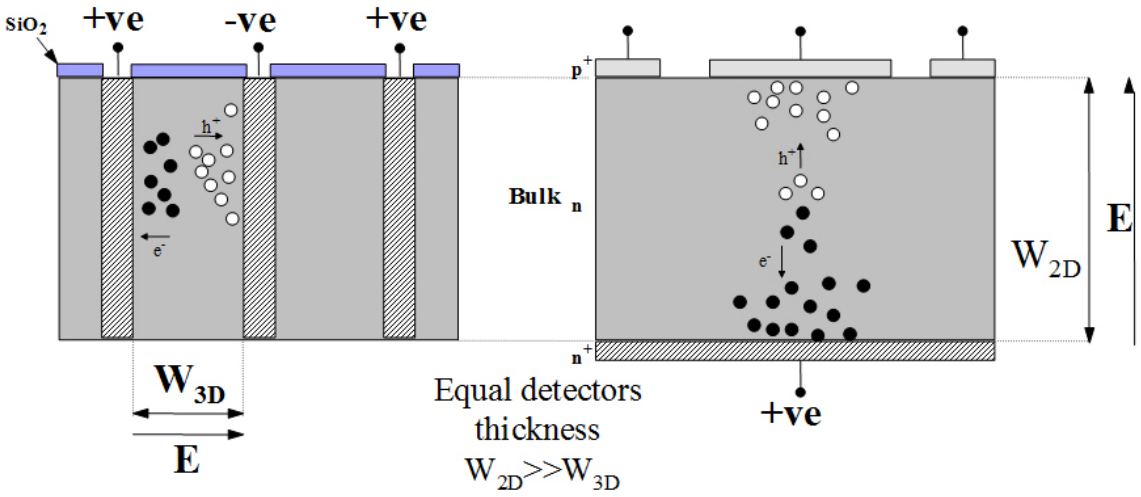

Figure 4.5: 3D (left) and planar (right) pixel silicon detectors [19]

Planar pixel detectors consists in an array of pixels in one side parallel to the surface. One problem in planar sensors is the charge sharing between neighbouring pixels (the e/h pairs created by the same particle are shared between two or more pixels). This problem is lowered in **3D pixel detectors** which have column-like

n+ and p+ electrodes perpendicular to the sensor's surface. Since the 3D electrodes can be closer than in planar sensor case, the full depletion voltage and noise are lowered.

Compared to traditional planar sensors, for which electrodes are processed on the wafer surface, both *3D designs have several important distinguishing features*:

- higher average electric field between the electrodes;
- a shorter collection path, implying a lower full-depletion voltage;
- advantages in extreme radiation environments.

The short electrode separation in 3D sensor (the typical inter-electrode distance is around 100 μm) gives more radiation hardness than the planar one to the sensor, making it a candidate for the LHC upgrade, the AFP project.

4.5 3D silicon detectors

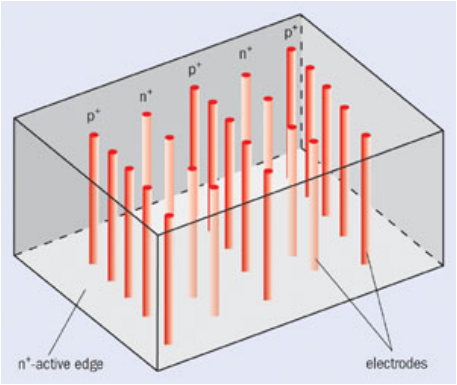

Figure 4.6: Schematic view of 3D sensor structure [19].

The 3D architecture was originally proposed by Parker et al. more then 10 years ago. The electrodes in 3D detectors are fabricated by etching holes in a silicon substrate, typically with Deep Reactive Ion Etching (DRIE), then filling them with polysilicon. This makes 3D sensors considerably more complicated to produce than traditional planar sensors.

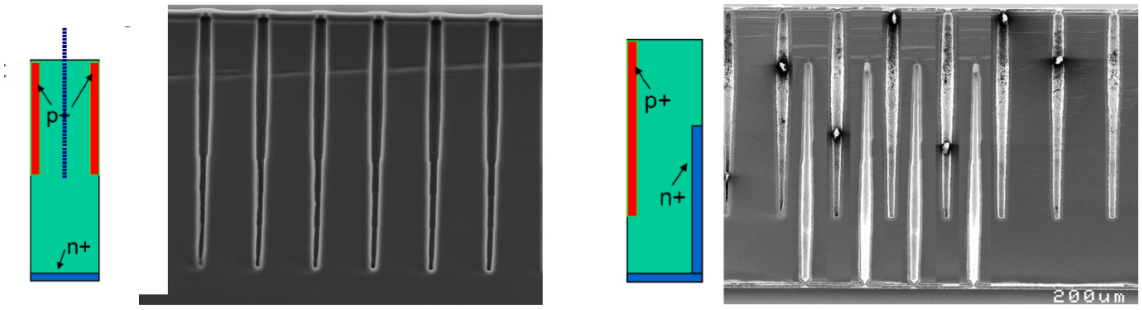

Figure 4.7: 3D sensor structure. **Left:** Full-3D structure, single column. **Right:** Modified 3D, double-sided structure. [19].

Different designs are currently under study: the Full-3D sensors fabricated at Stanford and in parallel at SINTEF with fully penetrating electrodes, and the modified 3D double-sided sensors fabricated by Fondazione Bruno Kessler (FBK) in Trento and by the Centro National de Microelectronica (CNM) of Barcelona, Spain in which the electrodes do not penetrate the entire substrate thickness.

4.5.1 3D sensors for AFP project

The 3D sensors for AFP project have been manufactured in two production facilities, CNM and FBK, with the same specifications. The sensors are produced on a 230 μm thick wafer with a double-sided process, i.e. the n^+ and p^+ type columns are etched from opposite sides of the substrate. The pixel configuration consists of two n-type readout electrodes connected at the wafer surface along the 250 μm long pixel direction, surrounded by six p-type electrodes which are shared with the neighboring pixels.

Schematically the CNM and FBK devices are presented in Figure 4.8. The CNM 3D sensor design features 210 μm long columns which are isolated on the n+ side with p-stop implants. The edge isolation is accomplished with a combination of a n+ 3D guard ring, which is grounded, and fences which are at the bias voltage potential from the ohmic side.

The FBK 3D sensor design presents pass-through columns isolated on the junction side with the p-spray technique. A 200 μm long ohmic fence isolates the pixel area from the edges the z direction. The sensor quality is evaluated before dicing using a

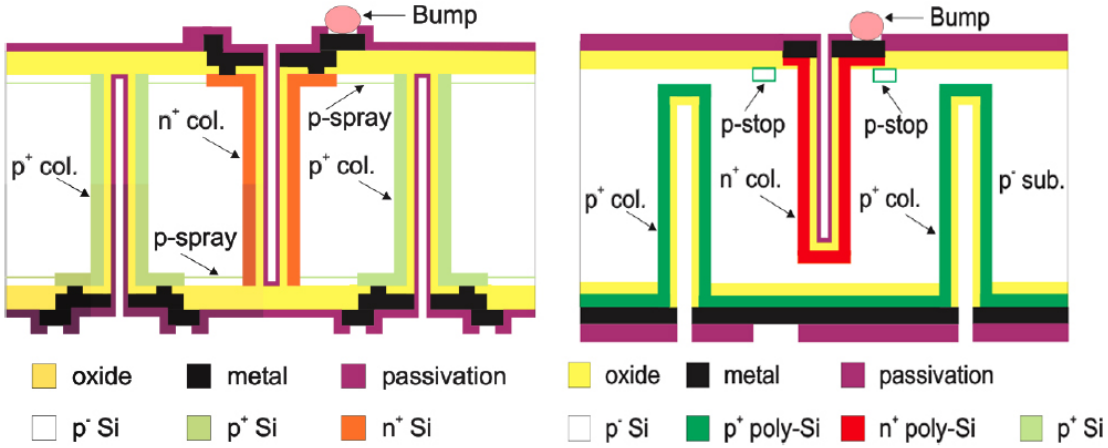

Figure 4.8: 3D double-sided sensor layout. **Left:** FBK (Trento, Italy), taken from [20]. **Right:** CNM (Barcelona, Spain), taken from [21]

temporary metal line that connects 336 pixels into strip. A total of 80 strips that are connected to a pad located outside the active region of the sensor, allow to evaluate the electrical characteristics of the device. After the measurements are completed the temporary metal layer is removed.

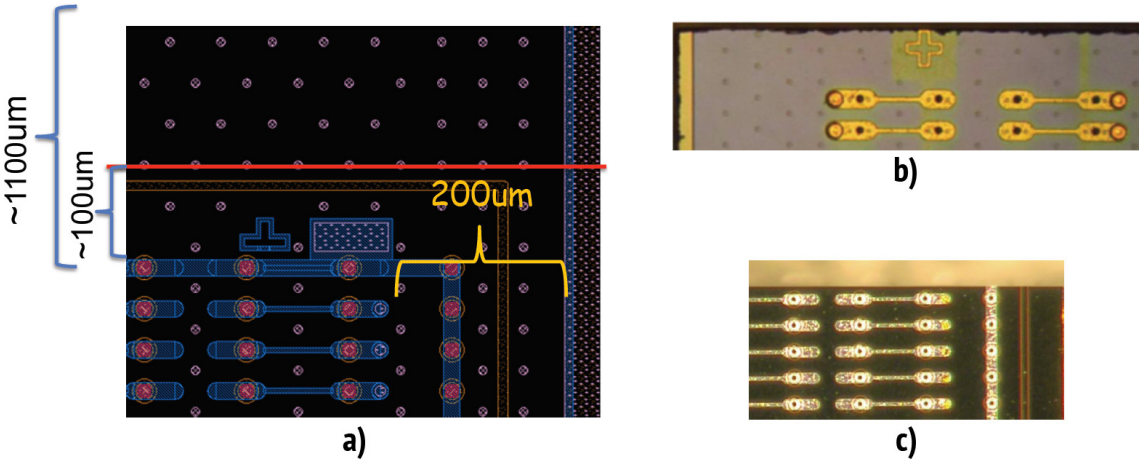

Figure 4.9: **a)** layout of uncut 3D sensor; **b)** diamond saw cut, FBK (dead area $\sim$ 100 μm); **c)** SCP method cutting, CNM4 (dead area $\sim$ 50 μm) [22].

The AFP project requires from the sensors the small dead space at the edge of the sensors (opposite wire bonds). For this purpose the 3D sensors was cutted. There are two ways of removing dead area:

- Standard diamond saw cut;

- SCP method (scribe-cleave-passivate).

For AFP inactive area of detectors was removed with diamond saw cut (see Figure 4.9).

Chapter 5

The Test Beam

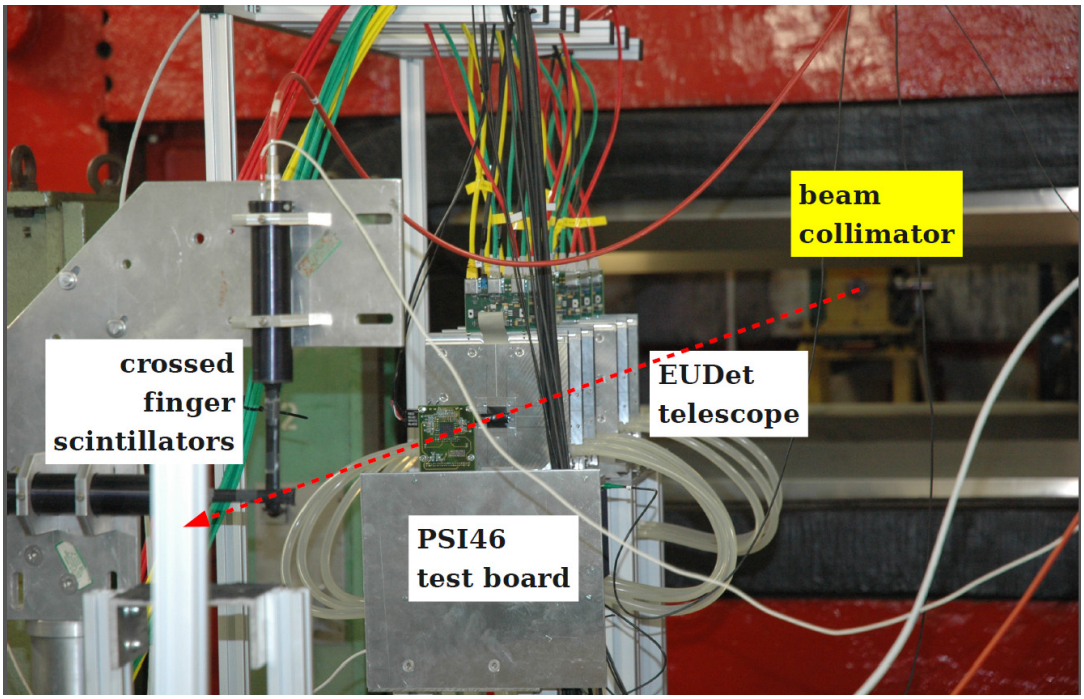

Figure 5.1: The test beam setup

Critical performance parameters, such as hit efficiency and position resolution, can only be determined at beam tests. Below the test beam setup used for this thesis is described in detail.

The 3D devices for the AFP project were studied at CERN in August 2012 and then in June 2013 at DESY. The CERN SPS North Area beam line H8 provides reasonably monochromatic π^+ pions with the energy of 120 GeV/c. DESY super-synchrotron machine provides e^+ positrons with energy

5 GeV/c. The trajectories of the beam particles are recorded using a reference system (beam telescope). Since the beam particles have a high $\beta\gamma$ factor they may be considered minimum ionizing particles (MIPs), and thus, the multiple scattering effects can be neglected. This allows to perform high precision tracking measurements.

Devices under test (DUT) were placed in the beam trajectory and using the telescope the track hit positions are obtained in the DUT planes. This information along with the information from the DUT itself and the arrival time of the particles allow to characterize the devices, estimating hit reconstruction efficiency and resolution, among other parameters.

The EUDET Pixel Telescope was used as a reference system for track measurements.

5.1 The EUDET telescope

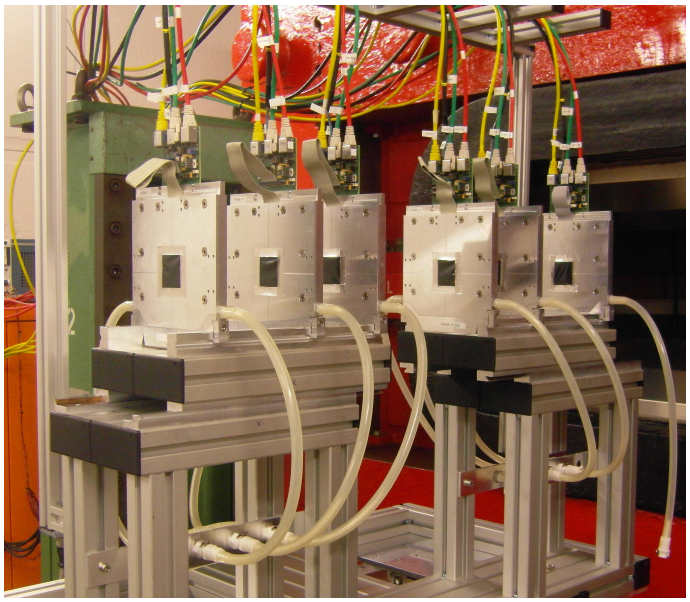

Figure 5.2: ANEMONE telescope, DESY beam line 21 [23].

The EUDET Pixel Telescope is designed for test beam operation. As shown in Figure 5.2 it consists of two arms, each equipped with three sensors (Mimosa26 pixel sensors) kept at a stable temperature by a cooling system. The positions of

the sensors along the beam axis can be adapted as necessary for a given application. Beetween the two arms, an optinal mechanical x-y support stage is installed, which allows positioning of the devices under test (DUTs) with a precision of a few micrometres.

The sensors used in the EUDET telescope is Mimosa26. The matrix of 576×1152 pixels cover an active area of $10.6 \times 21.2\ mm^2$ with a $18.4 \times 18.4\ \mu m^2$ pixel area.

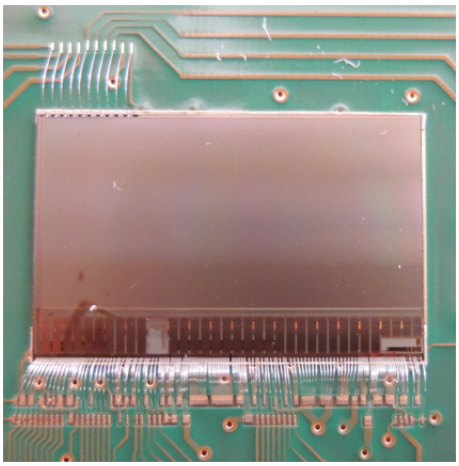

Figure 5.3: Mimosa26 pixel sensor [24].

5.2 Data acquisition system

The data from DUTs are read out by the USBpix System (see Figure 5.5) [25] and sent to the main DAQ PC. The telescope sensors are read out by the custom readout electronics that have been adapted to read out the fully digital MIMOSA-26 sensors. The maximum rate of the full setup with two VME crates reading out 3 Mimosa26 sensors each using the 80 MHz clock is about 800 Hz. The passage of particles are triggered using upstream and downstream mounts of two $1 \times 2\ cm^2$ scintillators at right angles. Triggering is controlled by a custom Trigger Logic Unit (TLU) that receives signals from the scintillators in front of and behind the telescope, and generates triggers that distribute to the telescope and any DUT.

A custom framework called EUDAQ is used for Data Acquisition (DAQ). It is flexible software that was designed to be modular and portable. The software makes use of several independent programs(producers) connected with each other over the

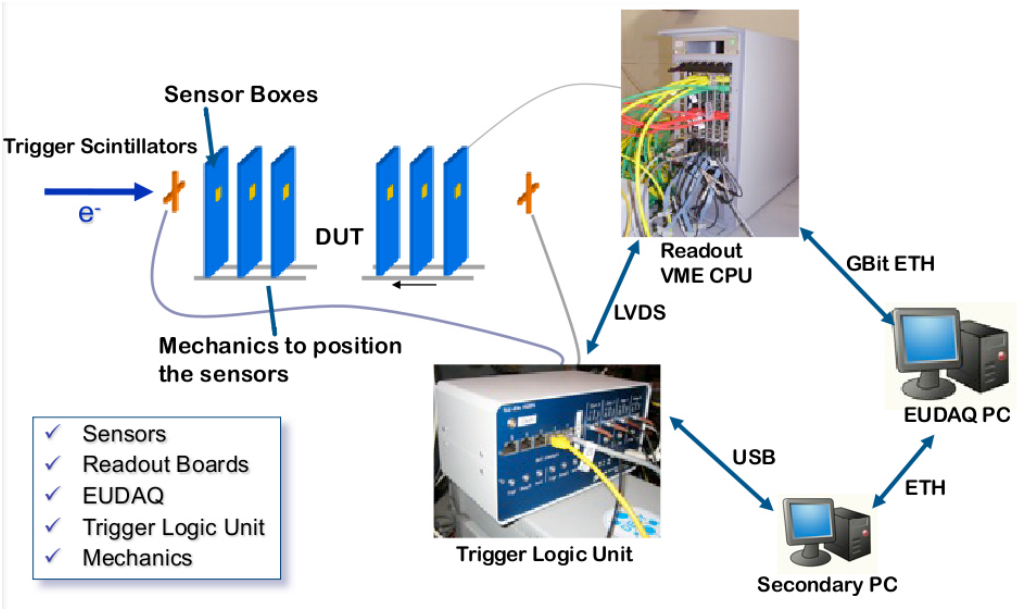

Figure 5.4: Sketch of DAQ system of the EUDET telescope [23].

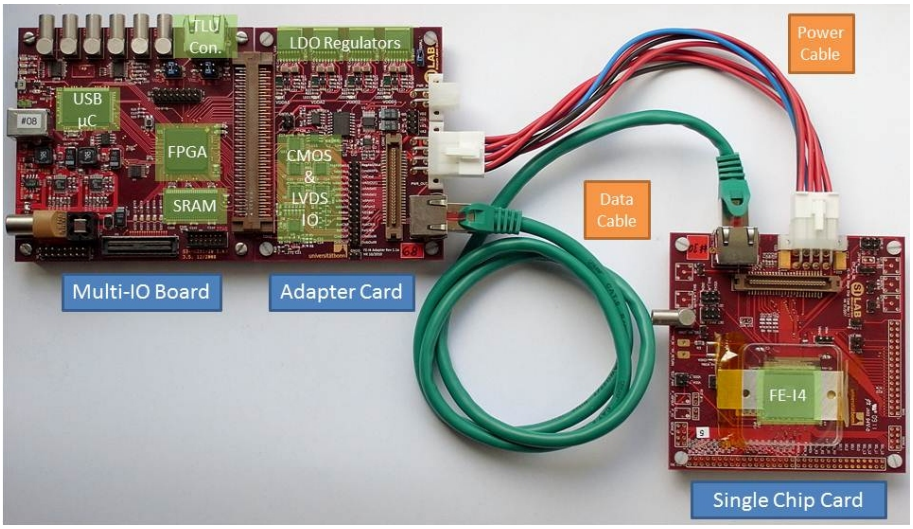

Figure 5.5: USBpix System and Front-end readout chip FE-I4 [25].

network. It provides a graphic interface to users allowing them to monitor the quality of data taking. The data recorded from the telescope and devices under test during one trigger are called event. A sequence of events without changes in the setup or re-initialization of the data acquisition system is referred to as run.

5.3 Analysis software EUTelescope

After the data taking and storage by the EUDAQ software the data-files have to be analyzed which is done by the EUTelescope software. The main goal of software is to reconstruct raw data to high level objects like tracks crossing the telescope. Those tracks are used to characterize both the telescope itself and any DUT inserted into the telescope setup, Like the data acquisition, the structure of EUTelescope software is very modular; each process performs a specific task on an input collection, providing an output collection that can be used by other processes. The current analysis chain used shown in Figure 5.6

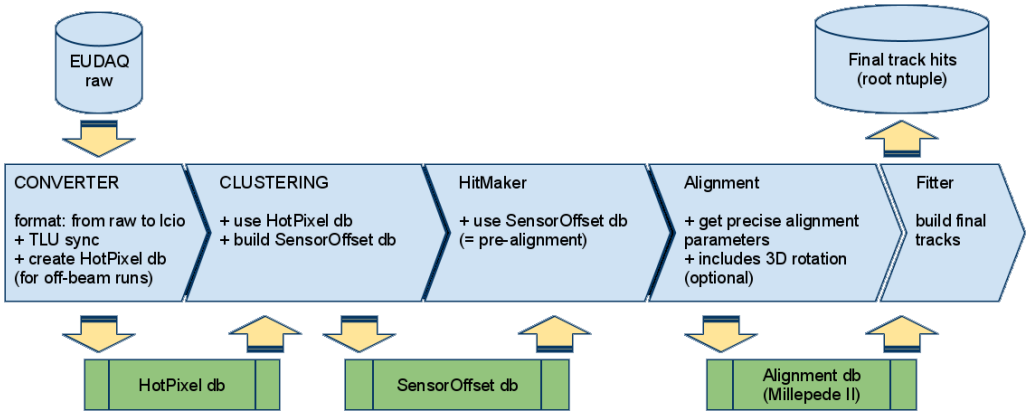

Figure 5.6: Data reconstruction steps [24].

5.3.1 Conversion

The first step in the EUTelescope analysis chain is the conversion of the raw data-formats into the Linear Collider Input/Output (LCIO) data-formats, which is necessary for the next analysis steps to work [23]. At this step, no information is dropped or added to the data. After conversion, the data are grouped by events. The information about the DUTs represents a set of data separated by a sensorID and consists of a sequence of hits represented by five entries per hit. These entries contain the information about the Column, Row, ToT (Time over Threshold), LVL1 Trigger and Readout Identification number of the hit.

When the raw data is converted to the LCIO format, the Format Converter processor generates a Hot Pixel database file containing the information about noisy

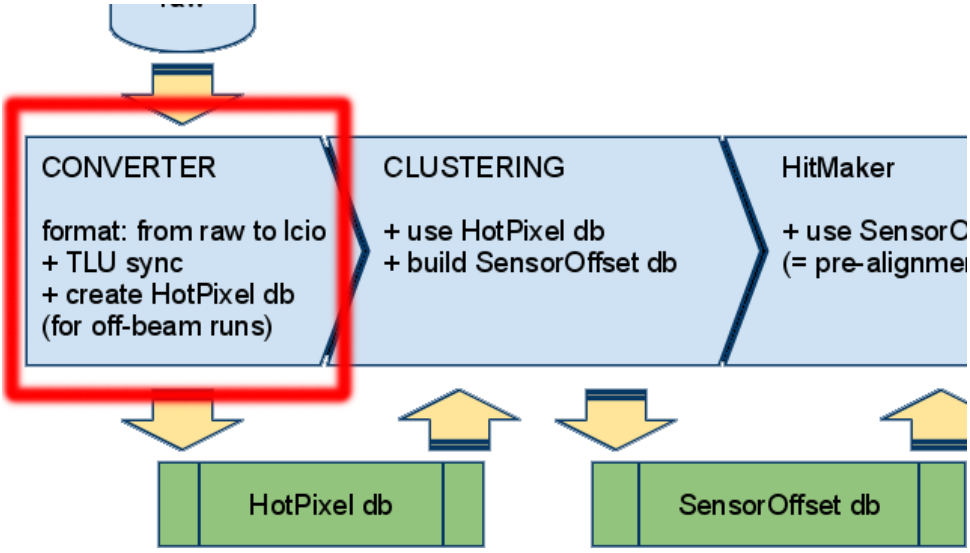

Figure 5.7: Data reconstruction steps. Converter [24].

pixels of the telescope and DUT planes.

5.3.2 Cluster search

After that a clustering algorithm tries to group pixel hits to a cluster. A cluster is a group of adjacent pixels that have fired. A pixel fires when the produced voltage-signal lies over a certain threshold. Thus a threshold is the amount of voltage above which pixels fire. When a particle passes through a sensor it may deposit energy in several pixels at the same time ("fired" pixels). The clustering algorithm groups these pixels together into objects called clusters.

In the default configuration, the nearest-neighbor search algorithm is used for clustering. It iterates through all fired pixels within the event and consolidates neighboring fired pixels into clusters. Each pixel may have up to 8 neighboring pixels. All fired neighbors for the given fired pixel are added to the current cluster and the clustering procedure is recursively applied to all fired pixels of the cluster until there are no fired neighbors. As a result, this recursive procedure ends by having grouped the neighboring fired pixels into disjoint clusters. After the clusters are marked out, the hit position is evaluated as a cluster center by a processor called Hit Maker.

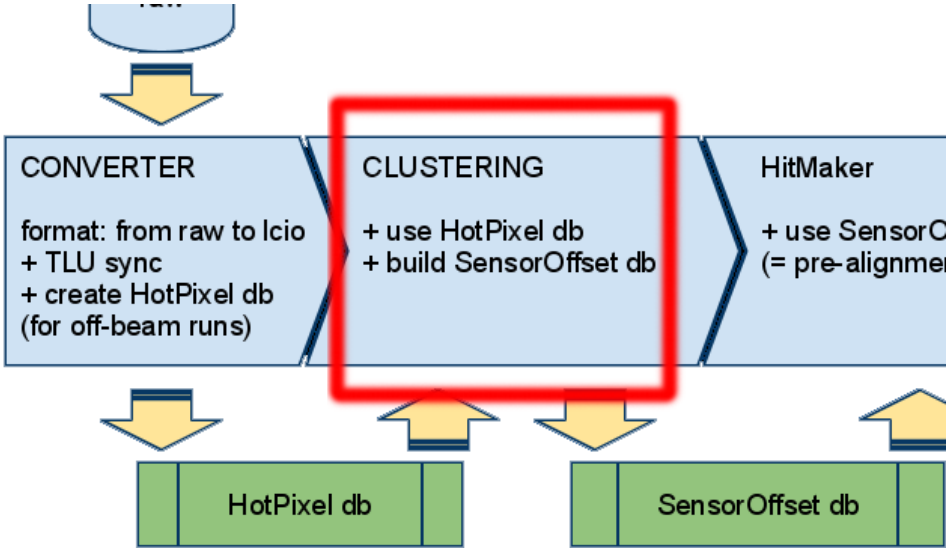

Figure 5.8: Data reconstruction steps. Cluster search [24].

5.3.3 Hit maker

After clusters are found by the clustering algorithm the hitmaker tries to define the hit position.

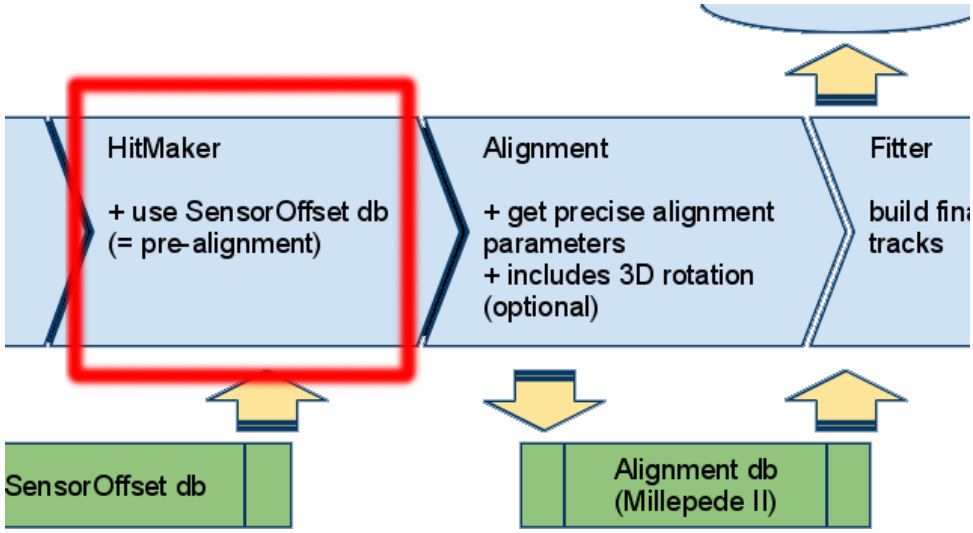

Figure 5.9: Data reconstruction steps. HitMaker [24].

There are several algorithms to calculate the hit-point position:

- **Cluster Weighted Center**

  The simplest method for calculating a cluster center is to take an average of the coordinates of the cluster pixels separately for X and Y. Since the fired

pixels coordinates are only known for the telescopes, this method is used to evaluate the hit position for clusters from telescope planes. Note, that if the cluster consists of one pixel only, the uncertainty of the telescope hit-point will be:

$$\sigma_{hit-point} = \frac{d_{pitch}}{\sqrt{12}} \approx 5.311 \mu m, \tag{5.1}$$

where $d_{pitch} = 18.4\ \mu m$ is the width of the square pixels of the telescope planes.

- **Cluster Charge Weighted Center**

  If the charge collection from the Time-over-Threshold information is available, one can use it to adjust the hit-point position for the cluster of the DUTs. This may be done by attaching the corresponding weights to the centers of the pixels and taking the center of mass of the obtained points as the hit-point position. HitMaker uses this method for the DUTs.

  Note that if the cluster consists of one pixel only, this method gives the same result as that Cluster Weighted Center. But if there are several hits inside the cluster, the resolution of the hit is expected to be better.

5.3.4 Alignment

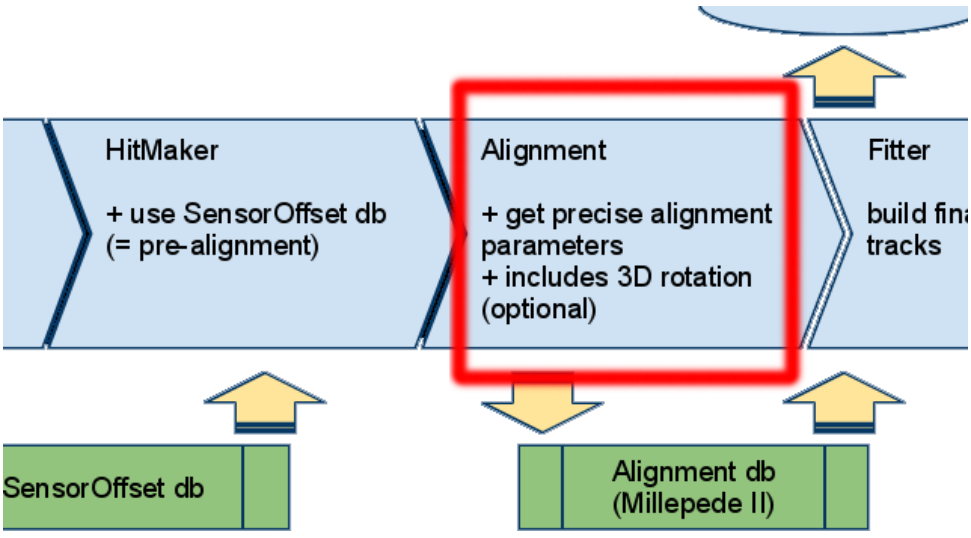

Figure 5.10: Data reconstruction steps. Alignment [24].

The fourth step of the analysis chain is the alignment. The imperfections of the mechanical alignment of the six sensor planes to each other have to be corrected. This is done on software basis via the Millepede II programme. The alignment uses a quick track fitter which identifies sensor hits belonging to the same track. This information is used to determine certain alignment parameters. In the analysis the alignment is done by fixing plane 0 and aligning the other planes with respect to this one [23].

5.3.5 Track fitting

The final step to reconstruct the particle trajectory is the track-fitting which uses the information from the hitmaker and the alignment analysis. Track reconstruction is performed by the Track Fitter processor which relies on the Deterministic Annealing Filter (DAF) for track reconstruction.

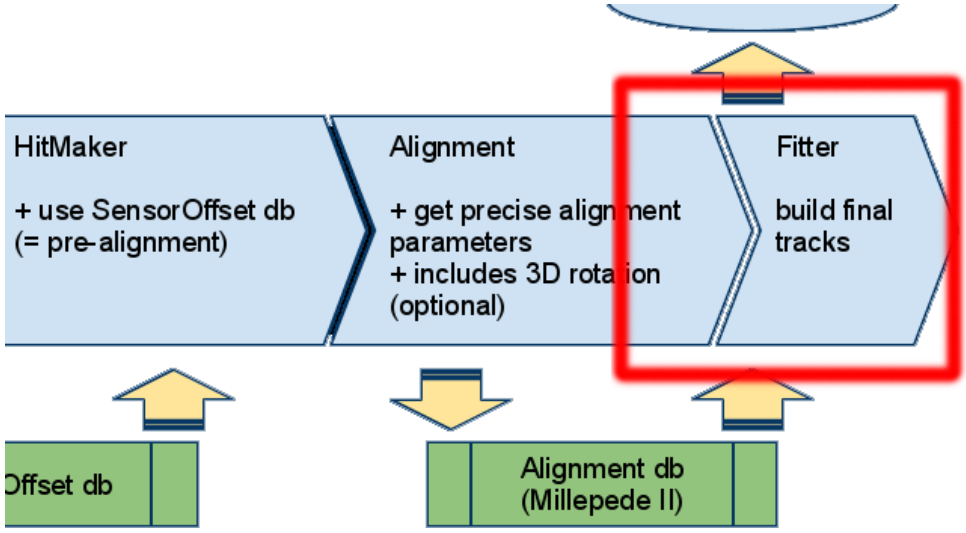

Figure 5.11: Data reconstruction steps. Fittering [24].

The DAF uses a χ^2-minimization that accounts for multiple scattering of impinging particle. Finding the minimal χ^2 is equivalent to solving a set of linear equations and can be done analytically.

5.4 Beam test measurements overview

In this thesis the results of the measurements performed during the August 2012 and June 2013 beam testing period at CERN and DESY respectively are presented.

The goal of these test beams is to evaluate the performance of different devices (3D sensors and readout electronics) under AFP conditions: small dead space at the edge of the sensors, non-uniform irradiation.

To increase the precision of detecting hit positions, the devices under test were placed between the telescope arms. Some of them were kept in a cooling box (August 2012 test beam at CERN) at an operation temperature of about -15^oC . The data were taken with the incident angle 0^o during both August 2012 and June 2013 test beams.

5.4.1 August 2012, CERN

In August 2012 at CERN, 3 devices for AFP project CNM-55, CNM-57, CNM-83 were tested. These devices are 3D double-sided silicon sensors, produced in Spain. All sensors were non cut (they had a normal for CNM 3D dead space on the edges around 1mm) and were mounted on the front-end readout chip FE-I4A, which was designed in 130 nm technology and features an array of 80 $\times$ 336 pixels with a pixel size of 50 x 250 μm^2.

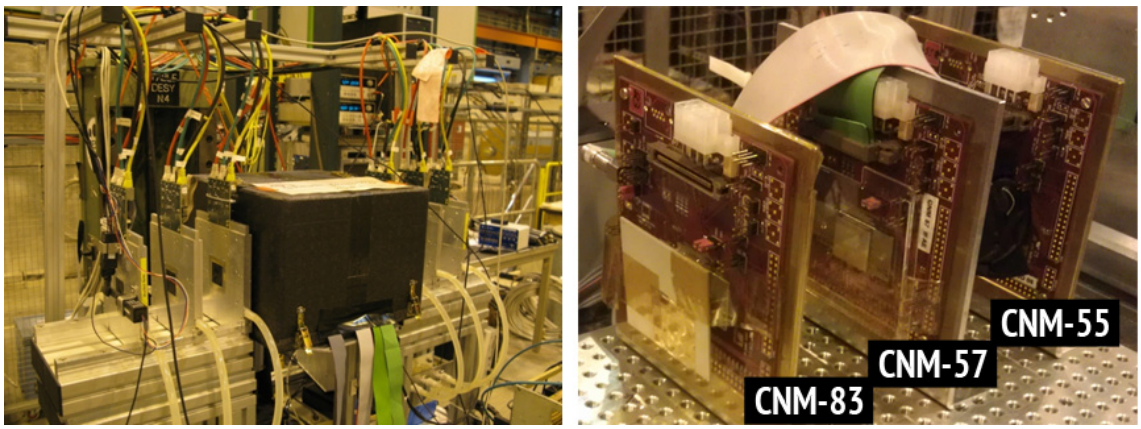

Figure 5.12: Left: EUDET Telescope, DUTs at cooling box (black). **Right:** DUTs, test beam August 2012.

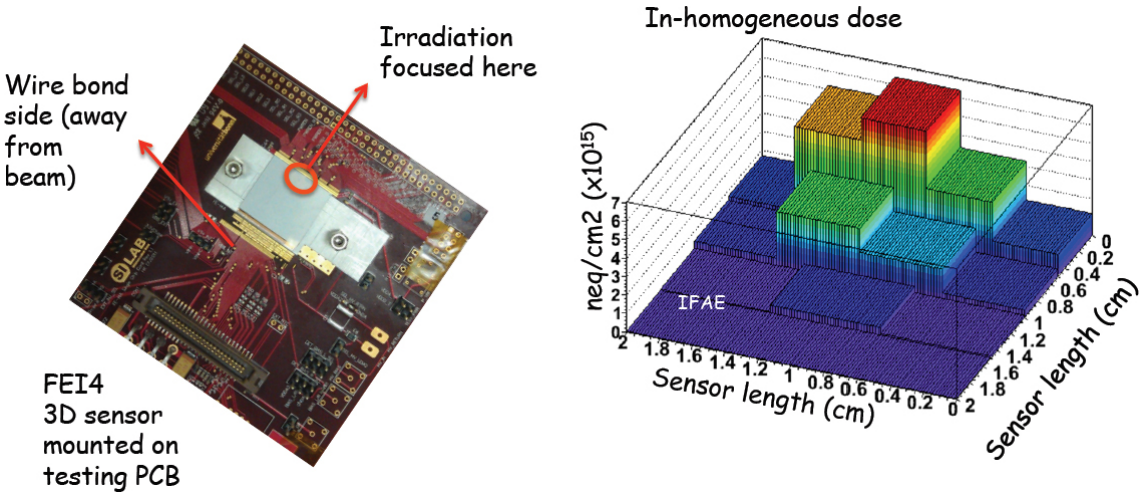

Figure 5.13: In-homogeneous radiation dose for CNM-57 and CNM-83 [26].

CNM-55 is a reference unirradiated sensor, CNM-57 and CNM-83 were irradiated by protons at IRRAD1 facility at CERN-PS by M. Glaser and P. Sicho. The samples were irradiated non-uniformly, see Figure 5.13. In this figure one can see, that non wire bonding side of the sensors was irradiated non-uniformly, and wire bonding side can be taken as unirradiated.

	DUT0	DUT1	DUT2
Sensor Type	CNM-55	CNM-57	CNM-83
Front-end	FE-I4A	FE-I4A	FE-I4A
Board ID	230	28	206
Fluency, $[n_{eq}/cm^2]$	unirrad.	irrad: $6.0 \cdot 10^{15}$	irrad: $1.0 \cdot 10^{15}$
Threshold, $[e^-]$	1700	1700	1700
Bias voltage [V]	-30	-130	-130

Table 5.1: DUTs configurations, test beam August 2012, CERN.

Table 5.1 describes the configurations which are studied dureing August 2012 CERN test beam. In this table the following legend was used:

- **Fluency:** the irradiation type and fluency of the sensor: unirradiated, irradiated.

- **Threshold:** the minimum charge (in number of electrons) that has to be collected by the device to fire the front-end discriminator.

5.4.2 June 2013, DESY

The goal of this test beam was to show that sensors with cut side still have good performance as sensors with not cut side, opposite wirebonds (see chapter 4).

In June 2013, four 3D double-sided designed silicon sensors with cut edge were tested: 2 CNM (produced in Spain): AFP_CNM_S3_R5, AFP_CNM_S5_R7 and 2 FBK (produced in Italy): AFP_FBK_S1_R9, AFP_FBK_S2_R10; and 1 reference detector CNM-55: 3D double-sided silicon sensors without cut edge, which was also used as a reference at August 2012 test beam described before. All these detectors were unirradiated.

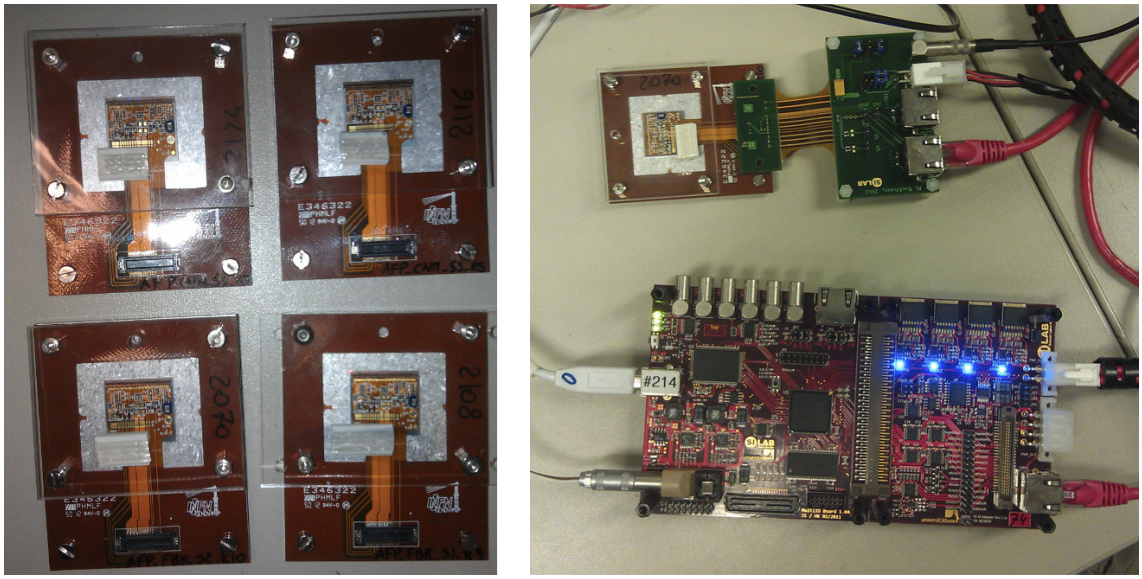

Figure 5.14: Left: DUTs, test beam June 2013. **Right:** Full setup FE-I4B chips with 3D sensors connected to the USBpix readout system.

All sensors, except CNM-55, were mounted on the new FE-I4B chips, which are not placed on Single Chip Boards (SCB can seen in Figure 5.5), but on the flexible cables. For connecting the FE-I4B chips to the USBpix readout system a special adapter developed at Bonn was used. Full setup can be seen in Figure 5.14 (right).

In order to be able to compare the performance of cut and uncut devices, all tested sensors were installed one by one, side by side with reference detector (CNM-55)

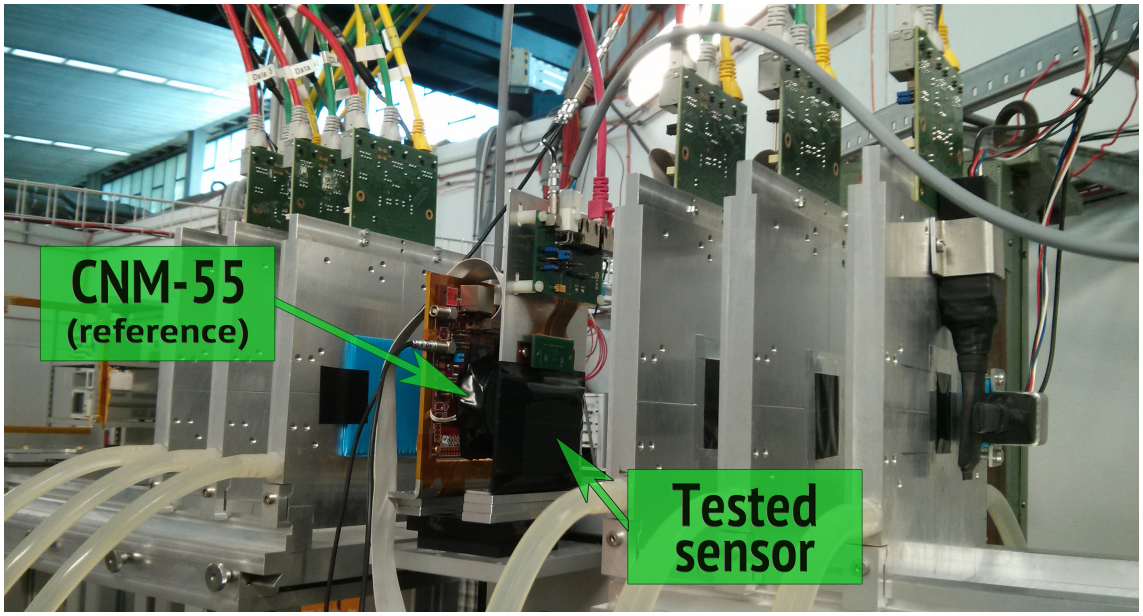

Figure 5.15: Reference and tested detector installed between the telescope plains.

and tested simultaneously at the test beam (see Figure 5.15).

Tables 5.2 - 5.5 describe the configurations of the batches from the June 2013 test beam.

Sensor Type	CNM-55	CNM_S3_R5
Front-end	FE-I4A	FE-I4B
Board ID	131	230
Fluency	unirrad.	unirrad.
Threshold, e^-	2800	1885, 1860
Bias voltage [V]	-30	-30

Table 5.2: DUTs configuration batch0, test beam June 2013, DESY.

Sensor Type	CNM-55	FBK_S2_R10
Front-end	FE-I4A	FE-I4B
Board ID	131	230
Fluency	unirrad.	unirrad.
Threshold, e^-	2800	1969
Bias voltage [V]	-30	-20

Table 5.3: DUTs configuration batch1, test beam June 2013, DESY.

Sensor Type	CNM-55	CNM_S5_R7
Front-end	FE-I4A	FE-I4B
Board ID	131	230
Fluency	unirrad.	unirrad.
Threshold, e^-	2800	1976
Bias voltage [V]	-30	-30

Table 5.4: DUTs configuration batch2, test beam June 2013, DESY.

Sensor Type	CNM-55	FBK_S1_R9
Front-end	FE-I4A	FE-I4B
Board ID	131	230
Fluency	unirrad.	unirrad.
Threshold, e^-	2800	2000
Bias voltage [V]	-20	-20

Table 5.5: DUTs configuration batch3, test beam June 2013, DESY.

Chapter 6

Data analysis

6.1 Offline analysis framework TBmon

TbMon is the offline analysis framework used by the 3D pixel and PPS groups. The schematical structure of TBmon is shown in Figure 6.1. Its main purpose purpose is to study the output ROOT files from the track reconstruction and to extract physics results, such as charge collection, tracking efficiency, device resolution, charge sharing between pixel cells, etc. TBmon allows to extract data from reconstruction files (TBtrack.root file), make specific cuts and calibrations, run different analyses and produce a set of desired plots for all specified devices under test [27].

TbMon assumes that the data is structured in configurations, which is generally corresponding to one experiment or testbeam period. One single configuration is built up of many runs, which are .root ntuples containing detector digits and tracking information. In addition to the ntuple files, a configuration is also consisting of event builders that handle data I/O for these ntuples, and sets cut flags on the events. The output of the event builders are an event object, which contains all the relevant information for the current event and DUT. These events are then passed on to one or more analysis, which makes plots, calculations etc. based on data accumulated for a single DUT [27].

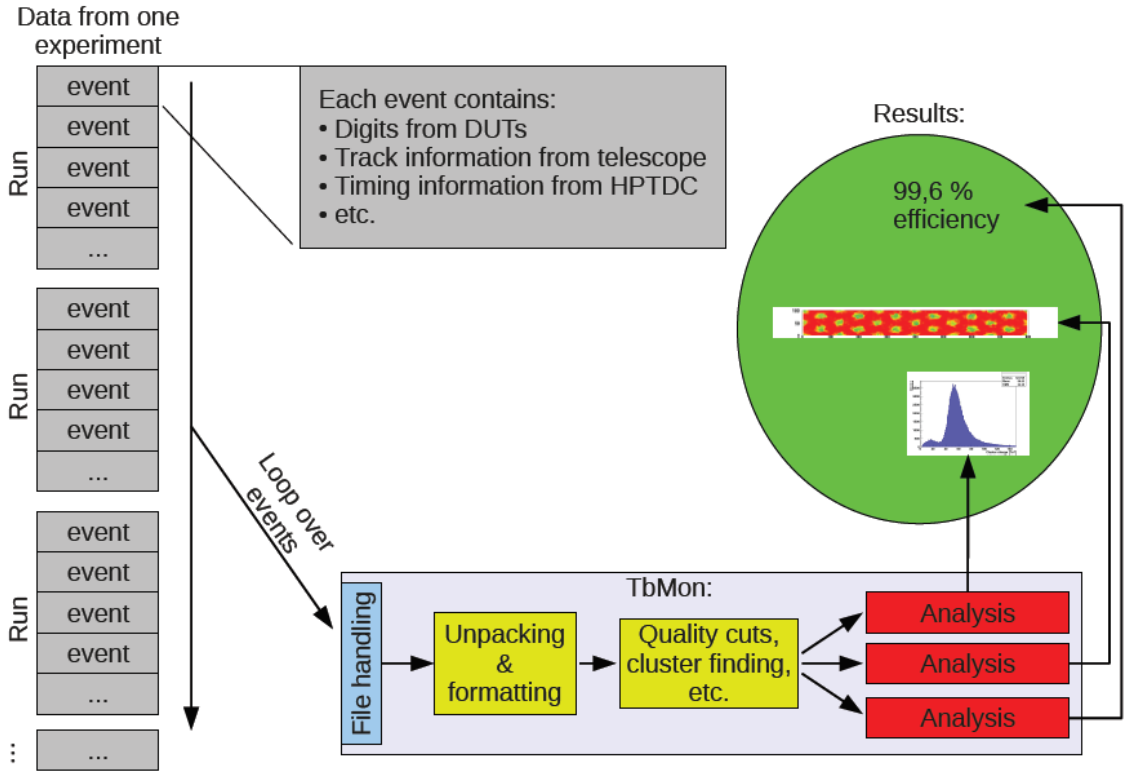

Figure 6.1: TBmon overview: Input, schematical internal structure and Output [27].

6.2 Data analysis overview

First of all a definition of used objects is in place:

- **Sensor Map** - a map of a sensor composed of pixels, each pixel being attributed a value of the parameter of interest and being colored according to that value. This kind of plot represents important characteristics of the experiment, such as beam profile, central and edge efficiency, etc. [28].

- **Pixel Map** - it shows cumulative distribution of some parameter mapped over the pixel area. It is helpful when exploring the behavior of the given parameter in the space between neighboring pixels [28].

The main analyses preformed for the devices are listed below. They are arranged from the simplest to the more sophisticated ones.

6.2.1 Beam profile sensor map

The beam profile plots show the beam position with respect to the DUT by showing the track position on the devices studied. Typically only part of the sensor is covered by the telescope area [28].

For example, during the June 2013 test beam each sensor was studied at two positions and from the beam profile you can learn which part of sensor is currently under study (see Figure 6.2).

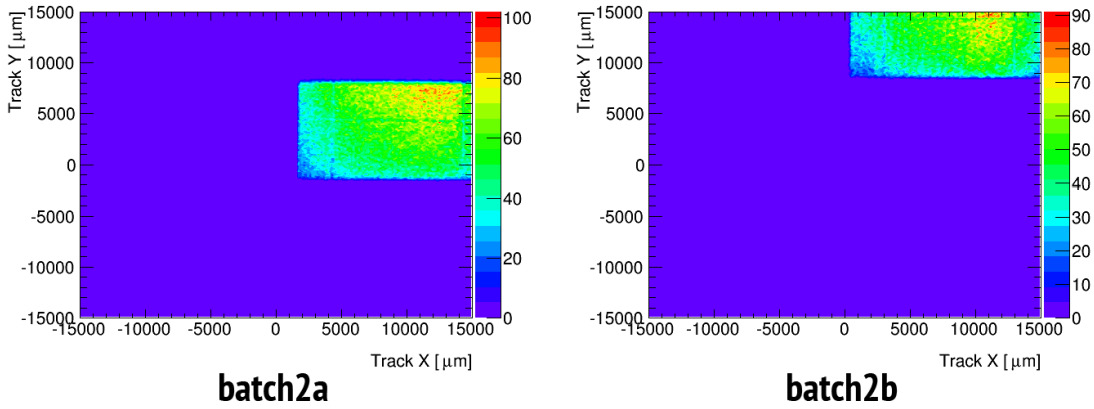

Figure 6.2: Beam profile sensor maps June 2013: **left**: batch2a, **right**: batch2b.

6.2.2 LVL1 trigger distribution

The LVL1 trigger distribution shows the number of readout events as a function of the time after the scintillator triggers initialize the telescope readout. This distribution gives an idea about time synchronization between the telescope and DUT planes. Devices are synchronized to start detecting the signal at around 5 LVL1 values, i.e. after 5×25 ns $= 125$ ns since the trigger from the scintillators arrives. The LVL1 values of noisy hits are evenly distributed so that they create a smooth plateau on the LVL1 trigger distribution plot. So this distribution also gives an idea about noisy hits [28].

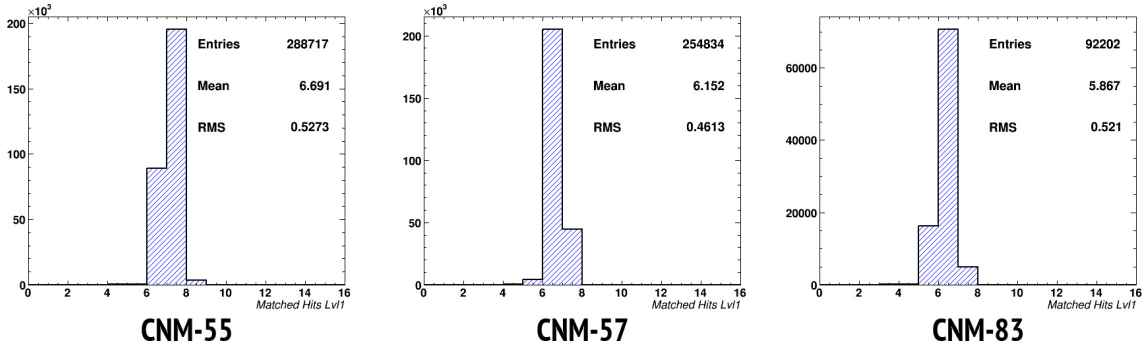

Figure 6.3: The LVL1 trigger distributions August 2012, non wire bonding side.

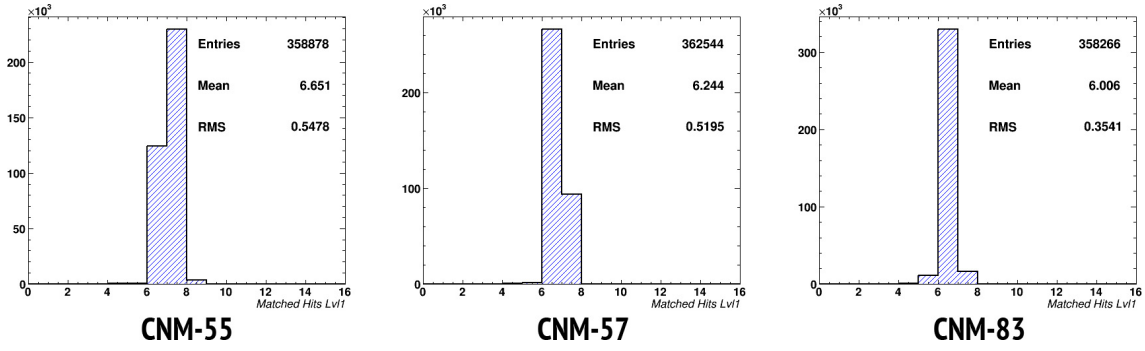

Figure 6.4: The LVL1 trigger distributions August 2012, wire bonding side.

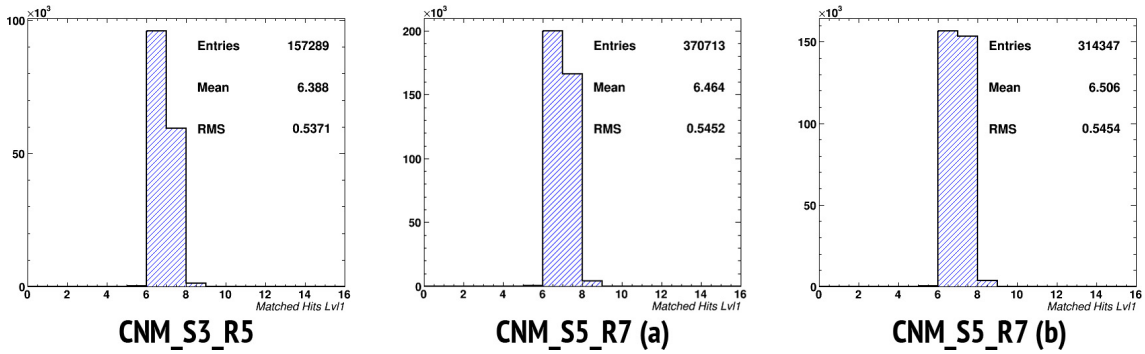

Figure 6.5: The LVL1 trigger distributions June 2013 test beam.

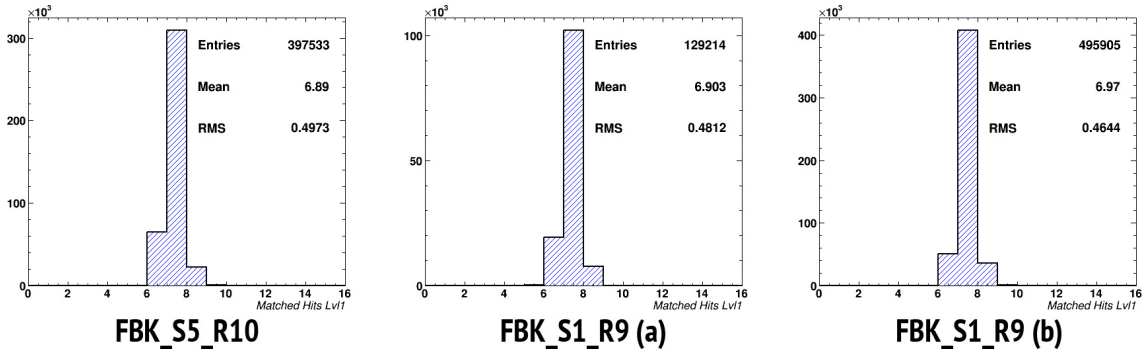

Figure 6.6: The LVL1 trigger distributions June 2013 test beam.

As we can see in Figures 6.3 - 6.6, there is not any plateau, which implies, that we don't have noisy hits, which indicates good system synchronization.

6.2.3 Cluster ToT spectrum distribution

The cluster ToT (Time over Threshold - the amount of time the signal exceeded the threshold value) spectrum is the distribution of the deposited charge (in ToT) of the detected particles.

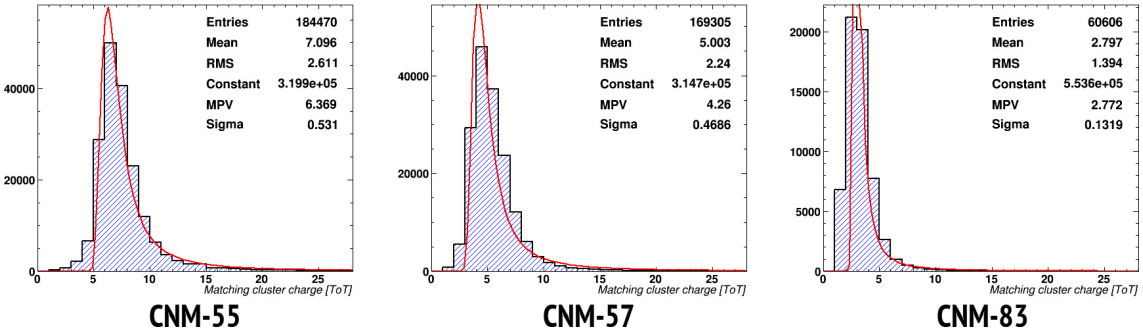

Figure 6.7: The cluster ToT spectrum distribution, August 2012, non wire bonding side.

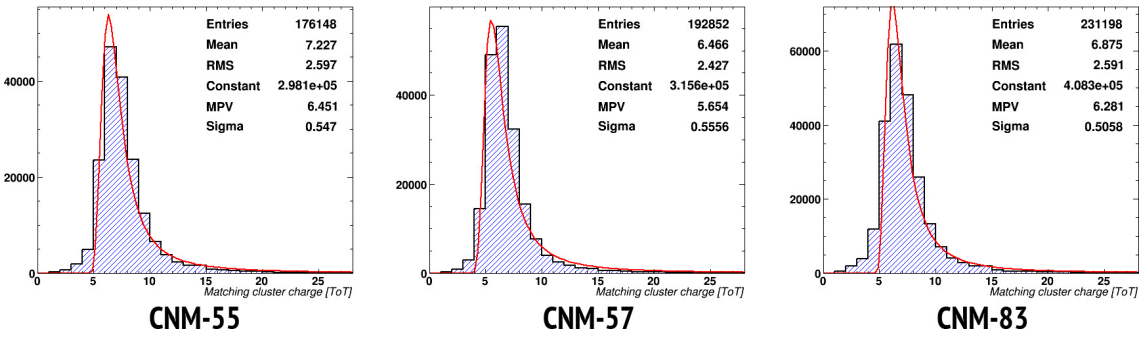

Figure 6.8: The cluster ToT spectrum distribution, August 2012, wire bonding side.

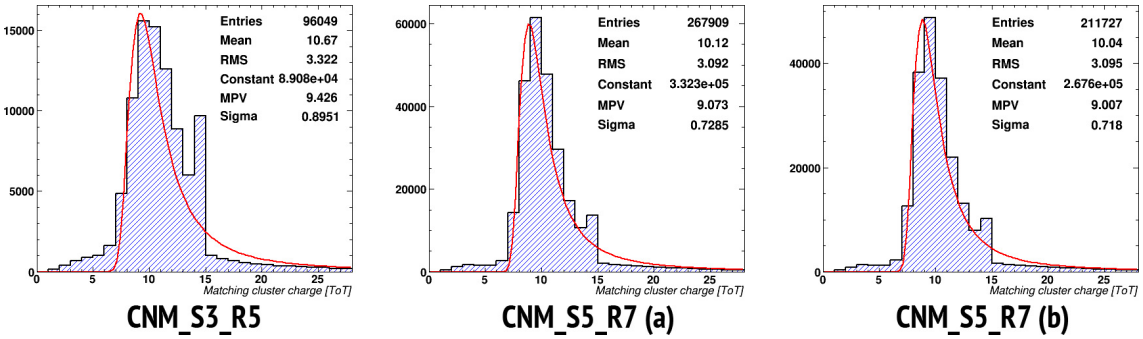

Figure 6.9: The cluster ToT spectrum distribution, June 2013 test beam.

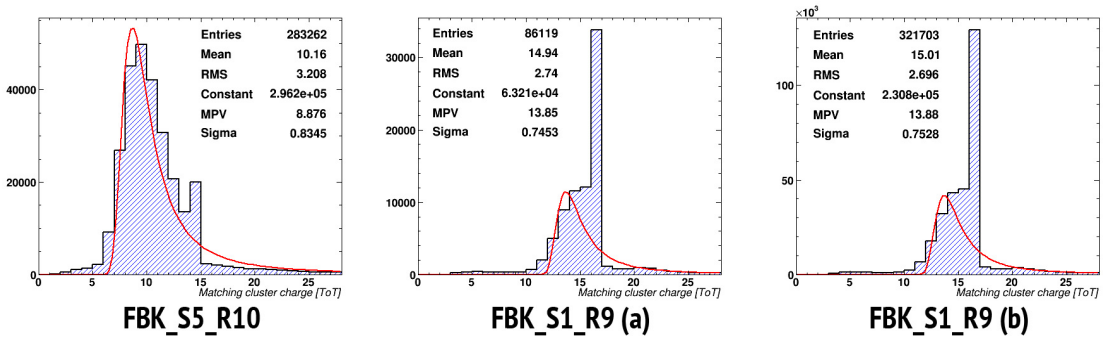

Figure 6.10: The cluster ToT spectrum distribution, June 2013 test beam.

The threashold values for each DUT can be found in Section 5.4. The ToT distribution follows a Landau distribution. It shows the number of readout events as a function of the ToT of the clusters [28].

In Figures 6.7 - 6.10, we can see that the MPV (most probable value) of the Landau distribution corresponds to threashold value (see Tables 5.1 - 5.5). The obtained cluster ToT spectrum distributions correspond to the expected values.

6.2.4 Cluster size distribution

The cluster size distribution is one of the important analyses for silicon detectors, in particular for the high η measurements and the measurements under the external magnetic field [28]. In this thesis the data were taken with the incident angle 0^o, that is why we expected mean cluster size around 1-2. Below are presented the matched cluster size distributions, where we can see mean cluster size around 1.25.

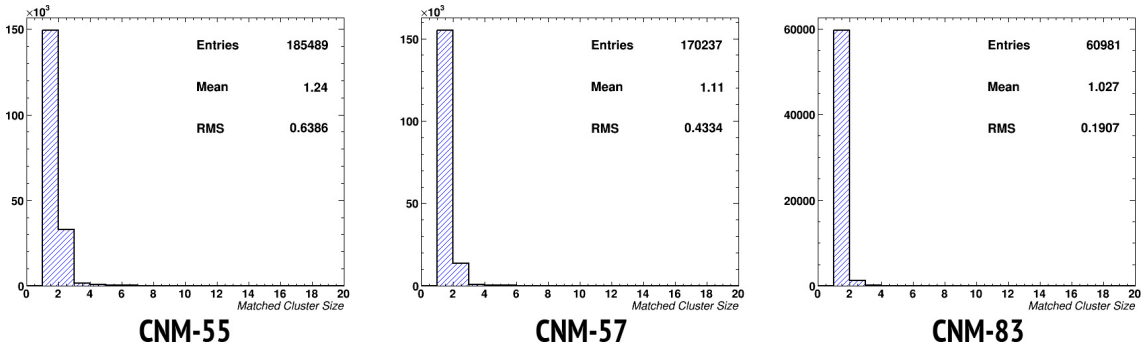

Figure 6.11: The matched cluster size distribution, August 2012, non wire bonding side.

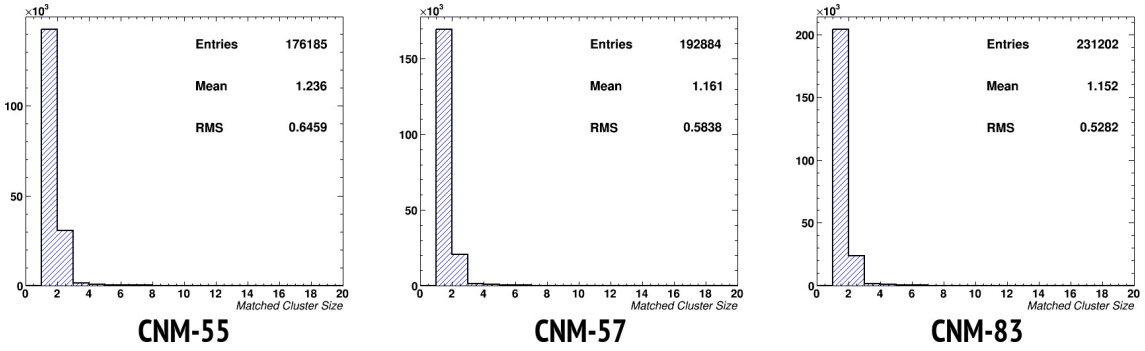

Figure 6.12: The matched cluster size distribution, August 2012, wire bonding side

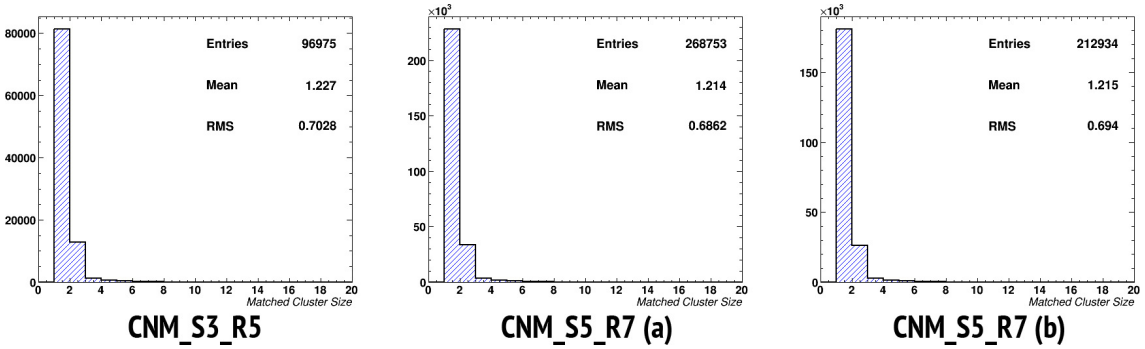

Figure 6.13: The matched cluster size distribution, June 2013 test beam.

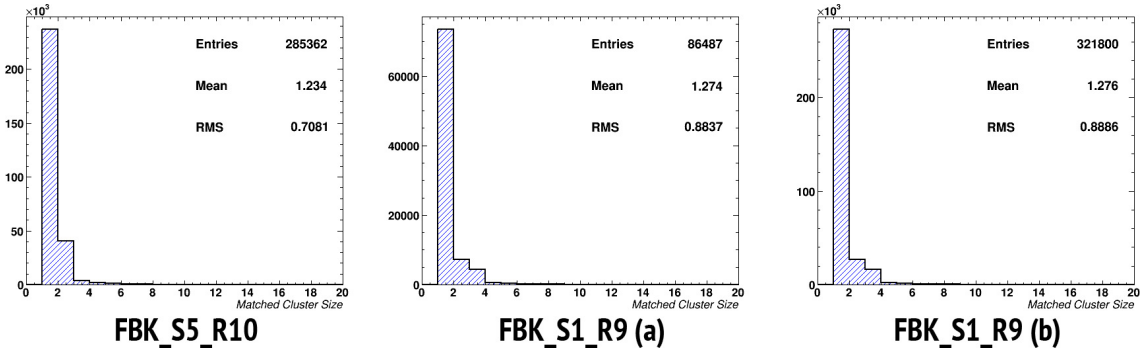

Figure 6.14: The matched cluster size distribution June 2013 test beam.

6.2.5 Sensor efficiency

Hit reconstruction efficiency is deffined as the probability of finding a hit close to the track. The covering area of the telescope plane is less than the covering area of the DUT ($10.6 \times 21.2\ mm^2$ versus $16.8 \times 20.4\ mm^2$) and since the tracks are reconstructed using the hits from the telescope planes only part of the DUT can be evaluated [28].

For a given device the tracking efficiency is calculated as a ratio of the Number of Matched Tracks and the Total Number of Tracks:

$$Efficiency = \frac{NumberofMatchedTracks}{TotalNumberofTracks}, \tag{6.1}$$

where

- **"Number of Matched Tracks"** corresponds to the fraction of the total number of tracks that are matched to a hit on the evaluated device.
- **"Total Number of Tracks"** is the number of reconstructed tracks that have matching hit on at least one other DUT (not the one being evaluated).

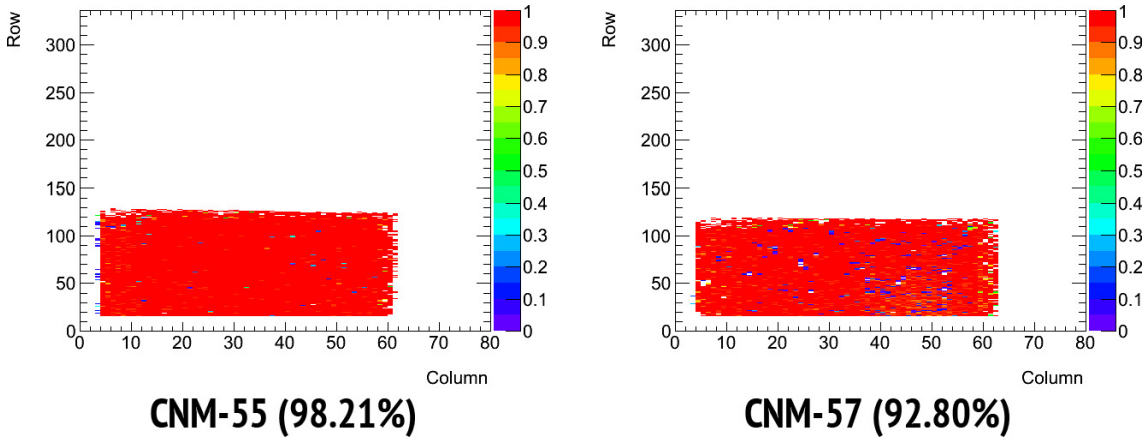

Figure 6.15: The efficiency sensor maps, August 2012, non wire bonding side.

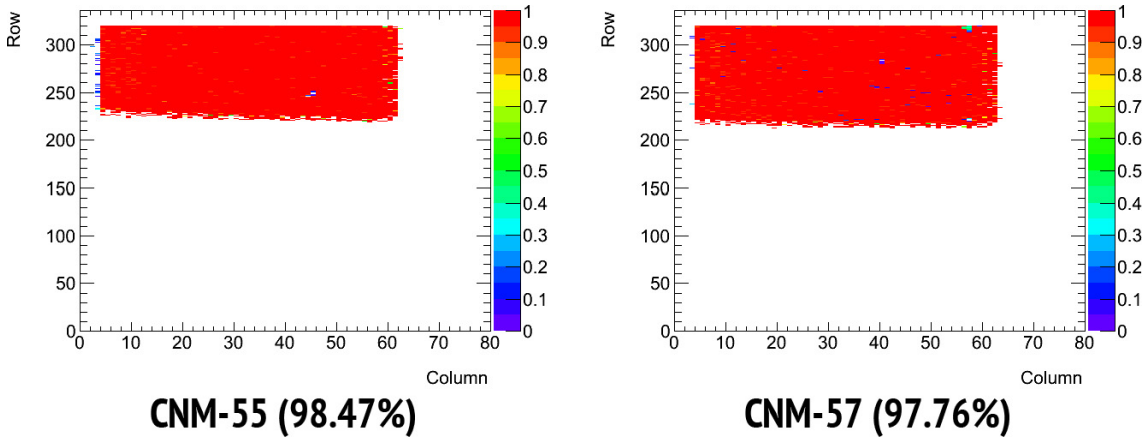

Figure 6.16: The efficiency sensor maps, August 2012, non wire bonding side.

Sample	Bias voltage [V]	Eff. WB [%]	Eff. non WB [%]
CNM-55	30	98.47	98.21
CNM-57	130	97.76	92.80
CNM-83	130	97.17	42.67

Table 6.1: The efficiency of the central region of the sensor from the test beam August 2012, CERN.

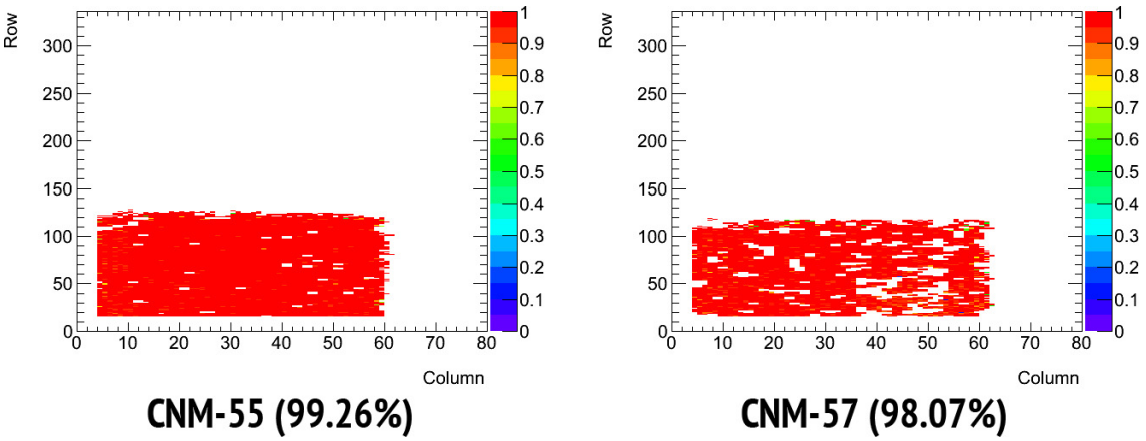

Figure 6.17: The efficiency sensor maps with masking of noisy pixels, August 2012, non wire bonding side.

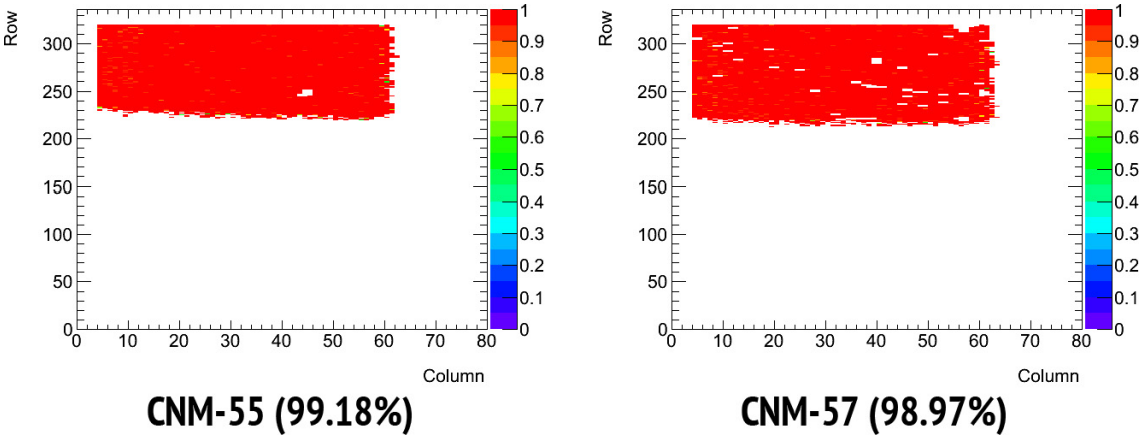

Figure 6.18: The efficiency sensor maps with masking of noisy pixels, August 2012, non wire bonding side.

Sample	Bias voltage [V]	Eff. WB [%]	Eff. non WB [%]
CNM-55	30	98.18	99.26
CNM-57	130	98.97	98.07
CNM-83	130	98.94	47.72

Table 6.2: The efficiency of the central region of the sensor with masking of noisy pixels from the test beam August 2012, CERN.

In Tables 6.1, 6.2 the following legend was used :

- **"Eff. WB"** corresponds to the efficiency of wire bonding side, unirradiated part of the sensor.
- **"Eff. non WB"** corresponds to the efficiency of non wire bonding side, irradiated part of the sensor.

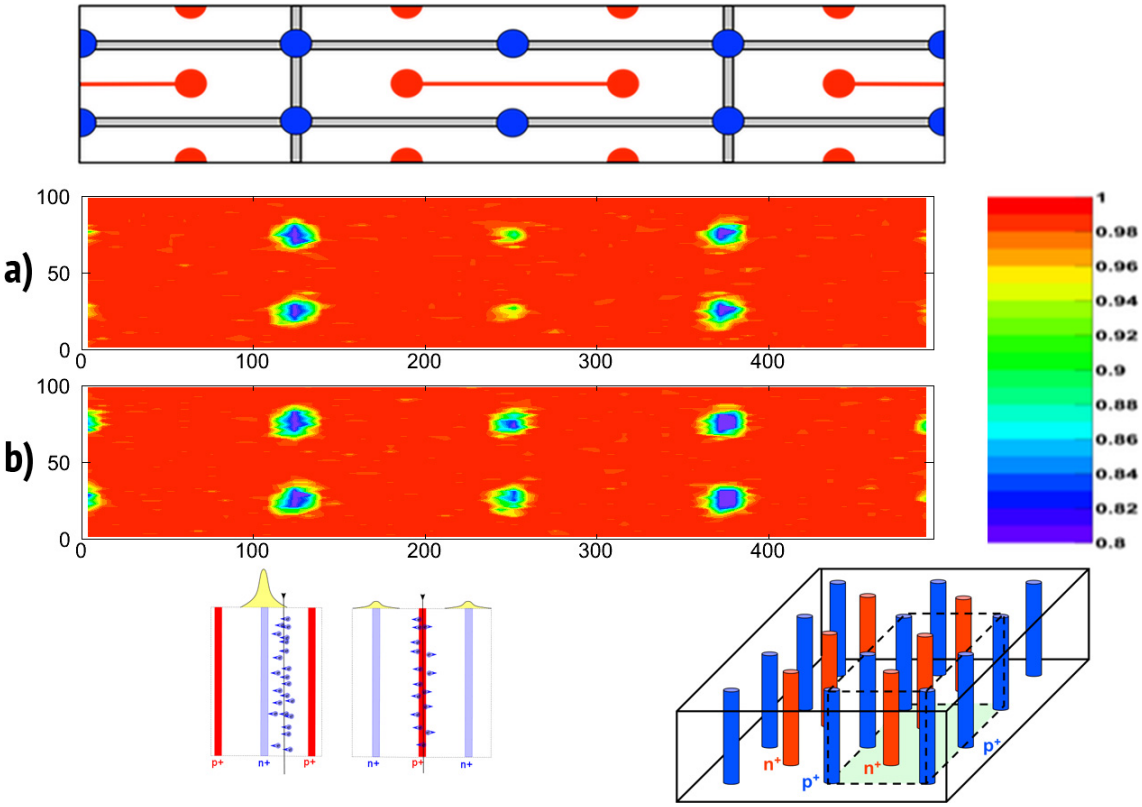

Figure 6.19: The efficiency pixel maps from the test beam August 2012: **a)** CNM-55, **b)** CNM-57 wire bonding side (unirradiated)

We can see, that non-uniformly irradiated sample still has good performance

compared to the unirradiated one. Both sides of the irradiated detector have good efficiency: 97.76% (unirr. part) and 92.80% (irr. part). It is understandable that irradiated sensor has more "hot" pixels (see Chapter 5.3). If we will mask the "hot" pixels and calculate the sensor efficiency with no respect to these "hot" pixels, we will get better results (see Table 6.2): 98.97% (unirr. part) and 98.07% (irr. part).

In Figure 6.19 we can see the structure of the 3D sensors and the efficiency pixel maps, on which the circles with low efficiency correspond to n^+/p^+ columns. These columns are not sensitive and affect the efficiency of the whole sensor area. That is why the efficiency of the reference detector CNM-55 is less than 100% ($\sim$ 99%).

When it has become clear from the results of the test beam data analysis (August 2012), that non-uniformly irradiated 3D sensors have good performance, let's look at the efficiency of the cut unirradiated sensors from the June 2013 test beam.

Sample	**Eff. non WB** [%]	**Eff. WB** [%]
CNM_S3_R5	-	98.29
CNM-55	-	98.63
CNM_S5_R7	96.98	96.97
CNM-55	98.20	98.29
FBK_S2_R10	98.54	-
CNM-55	98.56	-
FBK_S1_R9	93.35	93.50
CNM-55	98.14	98.20

Table 6.3: Efficiency of the central region of the sensors, test beam June 2013, DESY.

Table 6.3 presents the efficiency of the reference (CNM-55) and tested sensors for each batch of the June 2013 test beam. In Figure 6.20 can see, that cut sensors have not noise in cutting area, and good efficiency in these regions. Cutting didn't affect the performance of the detectors. In general, the devices have a good efficiency. If we look on the efficiency sensor maps of the FBK_S1_R9 device, we can see that

there are a lot of noisy pixels which affect the efficiency, but the edge region is still good and it is the most important parameter for our studies of the cut devices.

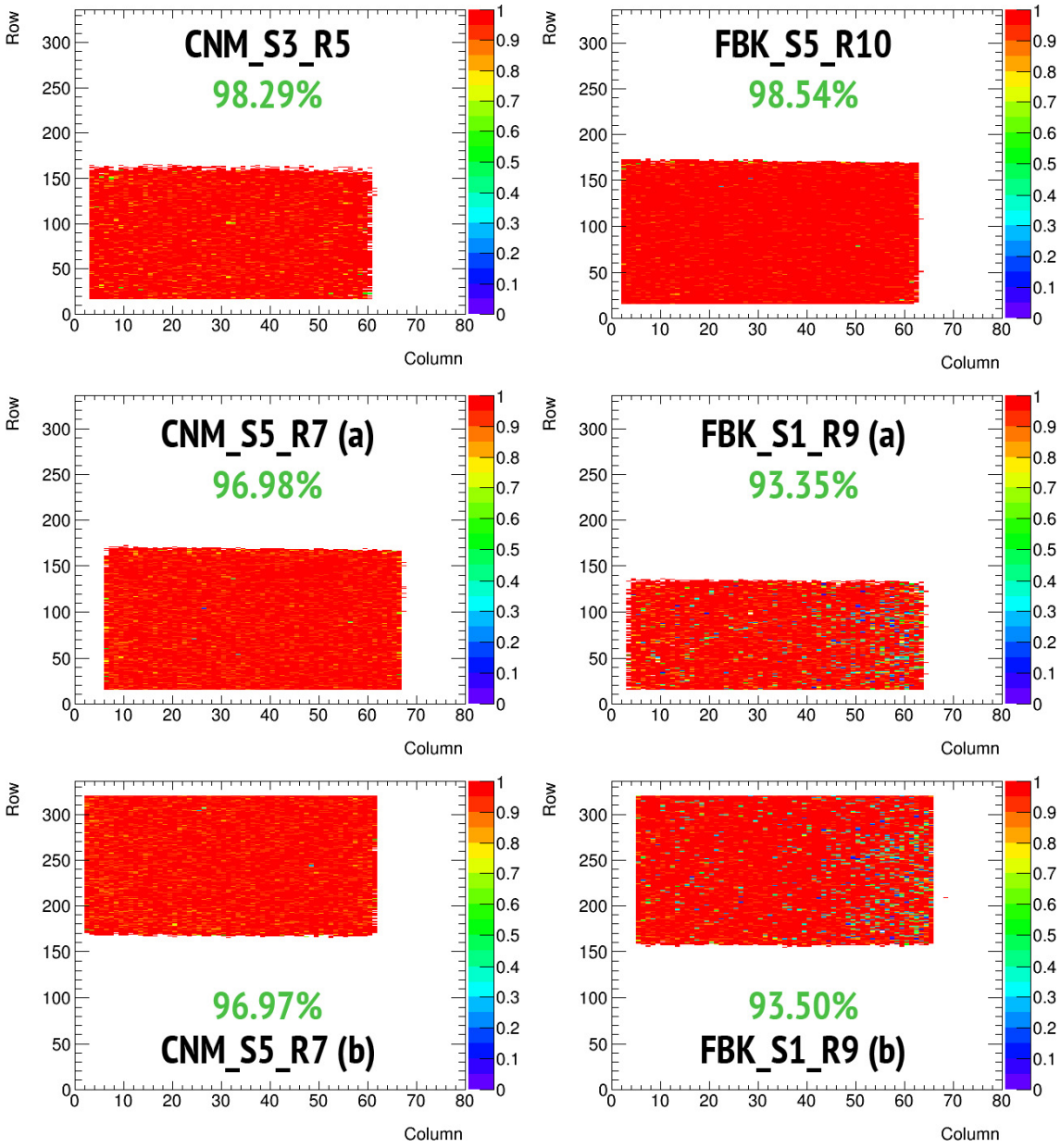

Figure 6.20: The efficiency sensor maps from the test beam June 2013, DESY.

6.2.6 Sensor position resolution

The position resolution for the devices under test is estimated separately for X and Y directions and is based on the evaluation of the residuals [28]:

$$Residual_{X,Y} = TrackPosition_{X,Y} - ClusterCenterPosition_{X,Y}. \quad (6.2)$$

There exist several algorithms to define the cluster center:

- **MaxToT:** the center of the cluster is selected at the center of the pixel with highest ToT value [28].
- η **- correction** - it shows cumulative distribution of some parameter mapped over the pixel area. It is helpful when exploring the behavior of the given parameter in the space between neighboring pixels [28].
- **Analog:** the center of the cluster is a mean position of the pixels in the cluster, without using the ToT information [28].
- **Digital:** the cluster center is the ToT weighted center of the cluster [28].

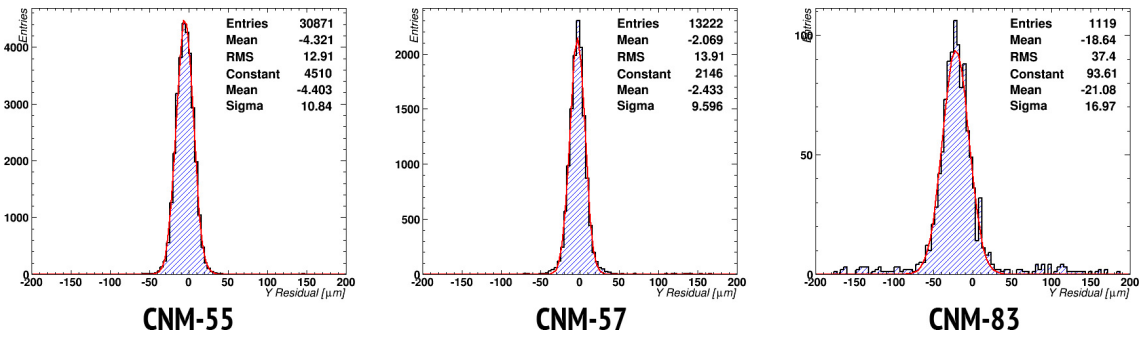

Figure 6.21: The residual distribution, August 2012 test beam, non wire bonding side

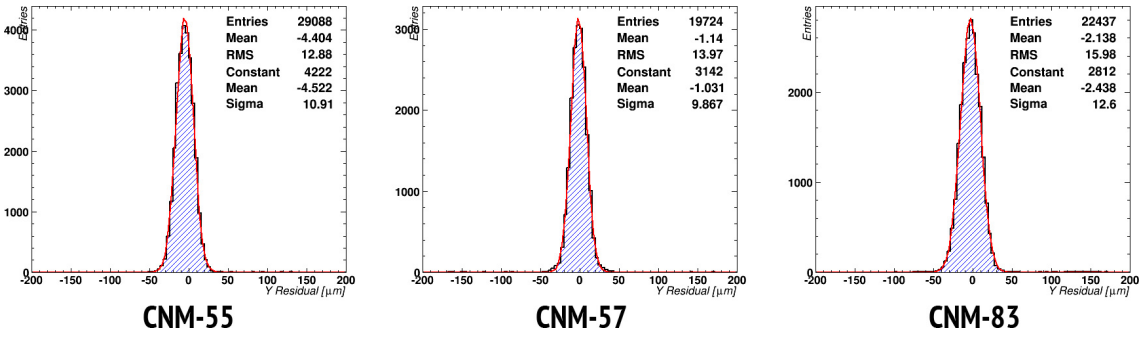

Figure 6.22: The residual distribution, August 2012 test beam, wire bonding side.

If a cluster consists of one pixel only, all these algorithms give equal results, and such clusters are of little interest [28].

In this thesis, the position resolution estimated from residual distribution in two-cluster hits (include ~ 3 μm telescope resolution (σ_{TEL}) is presented. The residual distributions follow a Gaussian distribution. Sigma (standard deviation) corresponds to the position resolution.

Taking into account the telescope resolution, one can obtain the approximate resolution for the sensors (σ_{DUT}) using Equation 6.3.

$$\sigma_{DUT} = \sqrt{\sigma^2 - \sigma_{TEL}^2} \tag{6.3}$$

In Figures 6.21, 6.22, we can see residual distribution for the sensors from the August 2012 test beam. Table 6.4 presents calculated position resolutions of these sensors. Note good position resolution of the reference (CNM-55) and non-uniformly irradiated (CNM-57) sensors.

Sample	**Pos res. non WB** [μm]	**Pos res. WB** [μm]
CNM-55	10.42	10.49
CNM-57	9.12	9.21

Table 6.4: The position resolution of the sensors, August 2012 test beam, CERN.

Sample	**Pos res. non WB** [μm]	**Pos res. WB** [μm]
CNM_S3_R5	-	21.84
CNM_S5_R7	15.67	16.09
FBK_S2_R10	15.05	-
FBK_S1_R9	15.90	16.11

Table 6.5: The position resolution of the sensors, test beam June 2013, DESY.

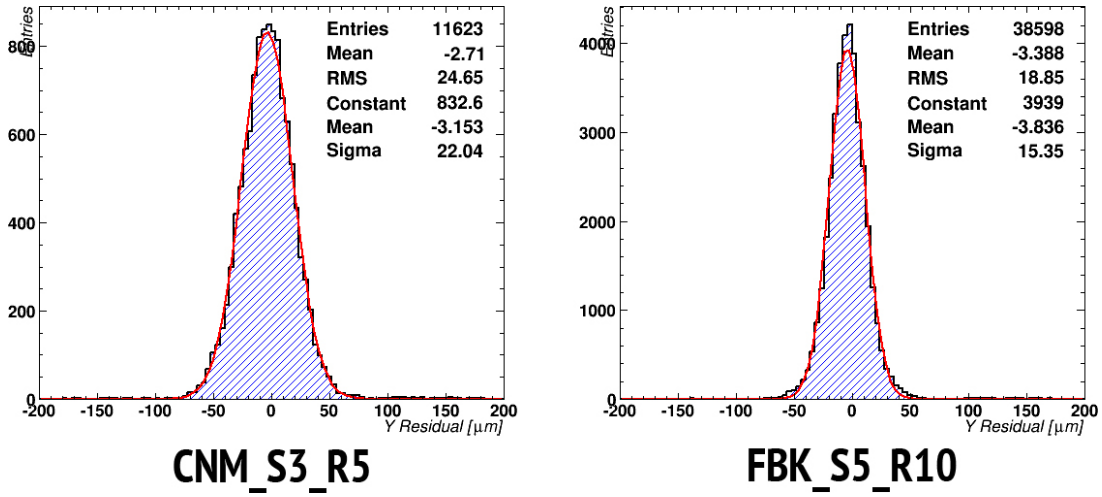

Figure 6.23: The residual distribution, test beam June 2013, batch0b, batch1.

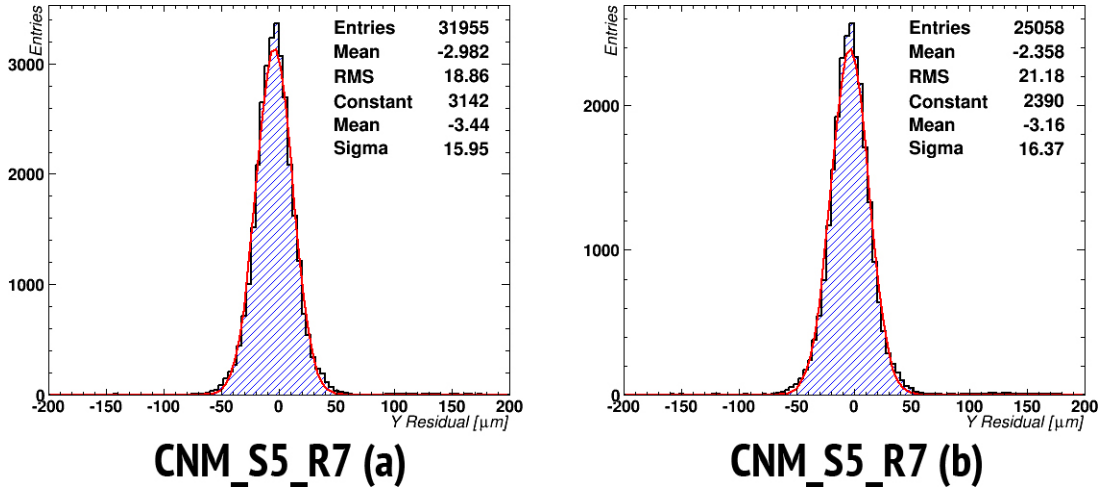

Figure 6.24: The residual distribution, test beam June 2013, batch2a, batch2b.

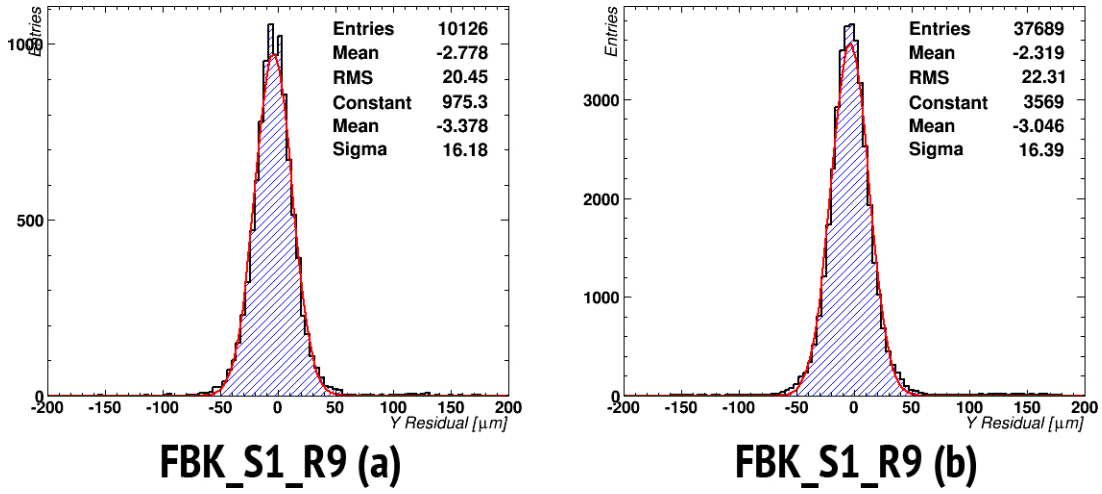

Figure 6.25: The residual distribution, test beam June 2013, batch3a, batch3b.

Table 6.5 presents position resolutions of the sensors from the June 2013 test beam. These values are larger than the values of position resolutions of the sensors from the August 2012 test beam at CERN. This is because the beam particles at DESY are 5 GeV/c positrons and at CERN - 120 GeV/c pions. At low energies the scattered effect is larger, which affect the residual distributions. The obtained results do not deviate from the expected values and therefore the evalueated sensors fulfill the requirements of the AFP project (30 μm).

Chapter 7

Conclusions

The goal of this thesis was to evaluate the performance of the new 3D sensors under the conditions that are expected during the AFP operation: small dead space at the edge of the sensors and non-uniform irradiation.

Two test beam irradiations were performed, first with a 120 GeV/c pion beam at CERN SPS beamline in August 2012, the second in June 2013, at DESY with 5 GeV/c positrons.

The non-uniformly irradiated 3D sensors were tested (CNM-57, CNM-83) at August 2012 with an unirradiated CNM-55 sensor used as a reference. During this test beam, the 3 devices under test were installed side by side and tested simultaneously on the beam with the help of a beam telescope.

During the second test at DESY, new 3D silicon devices with "slim" edge (dead space around 100 μm) were tested. On this test beam, two CNM (CNM_S3_R5, CNM_S5_R7) and two FBK (FBK_S1_R9, FBK_S2_R10) sensors were tested again with the CNM-55 used as a reference. In order to be able to compare the performance of the cut (slim edge) and uncut devices, all tested sensors were installed one by one, side by side with the reference detector and tested simultaneously on the beam.

During the preparation of this thesis the author participated in the August 2012 test beam at CERN and in the June 2013 test beam at DESY. The author performed the reconstruction and analysis of the data gathered from both test beams and the results are:

- **August 2012 test beam:** the 3D CNM-Barcelona devices meet the AFP

requirements in terms of hit reconstruction efficiency and position resolution after the non-uniform irradiation. For CNM-57, the efficiency of unirradiated side was around 98%, for irradiated side 93%. Position resolution in the Y direction (120 GeV/c pions) for unirradiated and irradiated sides was around 10.5 μm

- **June 2013 test beam:** it was indicated that cutting of one of the edges of the sensor did not affect the performance of the device.

In this thesis it was shown that the 3D silicon tracking detectors fulfill the requirements of the AFP project and can be installed in the AFP tracking stations.

The results of data analysis from June 2013 DESY test beam was presented on the "AFP Collaboration Meeting" at 10 July 2013.

The final test beam studies of the 3D silicon pixel sensors for the AFP project will be at March 2014.

Bibliography

[1] CERN web-pages for the general public. http://www.atlas.ch/fact-sheets-view.html. June 2013.

[2] The ATLAS Collaboration, "The ATLAS Experiment at the CERN Large Hadron Collider", JINST 3 (2008) S08003.

[3] The ATLAS Collaboration, "The ATLAS Inner Detector commissioning and calibration", 7 Jun 2010. [arXiv:1004.5293v2]

[4] ATLAS web-pages for the general public: http://atlas.ch/, June 2013.

[5] The ATLAS Collaboration, "ATLAS Muon Spectrometer Technical Design Report", CERN/LHCC 97-22.

[6] R. Staszewski†, "The AFP Project", Institute of Nuclear Physics Polish Academy of Sciences, arXiv:1104.1858v1 [physics.ins-det] 11 Apr 2011

[7] L. Adamczyka, R. B. Applebyb,c, P. Bankad, M. Boonekampe, A. Brandtf, P. Bussey, "AFP: A Proposal to Install Proton Detectors at 220m around ATLAS to Complement the ATLAS High Luminosity Physics Program". May 5, 2011

[8] ATLAS web-pages for the general public. https://home.web.cern.ch/, June 2013.

[9] Petr Sicho, "Silicon tracker for AFP", AFP Collaboration meeting (14.05.2013).

[10] CDF Collaboration, "Observation of Exclusive Dijet Production at the Fermilab Tevatron p-pbar Collider" Phys. Rev. D77 (2008) 052004.

[11] R. Staszewski and J. Chwastowski, “Transport Simulation and Diffractive Event Reconstruction at the LHC“, [arXiv:0906.2868].

[12] M. W. Krasny, J. Chwastowski, K. Slowikowski, “Luminosity measurement method for LHC: The Theoretical precision and the experimental challenges”, Nucl. Instrum. Meth. A584 (2008) 42-52.

[13] N. Schul, K. Piotrzkowski, “Detection of two-photon exclusive production of supersymmetric pairs at the LHC”, Nucl. Phys. Proc. Suppl. 179-180 (2008) 289-297.

[14] O. Kepka, C. Royon, “Anomalous WW gamma coupling in photon-induced processes using forward detectors at the LHC”, Phys. Rev. D78 (2008). 073005.

[15] E. Chapon, C. Royon, O. Kepka, “Anomalous quartic $WW_{\gamma\gamma}$,$ZZ_{\gamma\gamma}$, and trilinear WW_{γ} couplings in two-photon processes at high luminosity at the LHC”, Phys. Rev. D81 (2010) 074003.

[16] Ivan Lopez Paz, ”Characterization of CNM 3D FE-I3 Devices“, February 2012.

[17] C. Kittel, H. Kroemer, ”Thermal Physics“, W. H. Freeman and Company,2nd ed, January 15, 1980

[18] Rivero Fabio, ”Characterization of FBK-irst 3D Double Side Double Type Column Silicon Sensors“, 2008-2009

[19] M. Krammer, ”3 Detector Structures“, XI ICFA School on Instrumentation. Avail. July 2013.

[20] A. Zoboli et. al., ”3D Irradiation Results - Vertex” IEEE TNS 55(5) (2008), 2775.

[21] G. Pellegrini et. Al., “Status production of 3D at CNM“, NIMA 592(2008), 38.

[22] Sebastian Grinstein, ”Overview of Silicon Pixel Sensor Development for the ATLAS Insertable-B-Layer (IBL)“, IEEE Nuclear Science Symposium (NSS), 22-30 October 2011, Valencia, Spain.

[23] Illia Khvastunov, "Database for EUTelescope: making life easier", September 7, 2011.

[24] Igor Rubinskiy, "An EUDET/AIDA pixel beam telescope for detector development", CERN, 15 February 2012

[25] M. Backhaus et al., "Development of a versatile and modular test system for ATLAS hybrid pixel detectors", Nucl. Instrum. Meth. A650 (2011) 57; 37-40. International Workshop on Semiconductor Pixel Detectors for Particles and Imaging 2010.

[26] A. Micelli, S. Tsiskaridze, I. Lopez, A. Jimenez and S. Grinstein, "Non Uniform Irradiation of CNM", 21st RD50 Workshop, November 2012.

[27] Kyrre Ness Sjøbæk, "Full simulation of a testbeam experiment including modeling of the Bonn Atlas Telescope and Atlas 3D pixel silicon sensors", September 2010.

[28] S. Tsiskaridze and S. Grinstein, "Beam Test Results of the CNM-3D Devices for the ALTAS-IBL Detector", April 16, 2012.

[29] Jorn Grosse-Knetter, "Vertex Measurement at a Hadron Collider - The ATLAS Pixel Detector", BONN-IR-2008-04.

[30] D. G. d'Enterria, "Forward Physics at the LHC" [arXiv:0708.0551 [hep-ex]].

[31] R. Staszewski, "AFP project", Institute of Nuclear Physics Polish Academy of Sciences, 11 Apr. 2011.

[32] CERN-THESIS-2010-045, 06/11/2009.

[33] M.S. Alam, et al., Nucl. Instrum. Methods Phys. Res. A 456, 217 (2001).

[34] C. Kenney et al., "Comparison of 3-D and planar silicon detectors", in Proc. 9th Meeting Division Particles Fields of therican Physical Society, Minneapolis (MN), USA, Aug. 11-15, 1996, pp. 1342-1345.

[35] I.Rubinskiy. EUDET-Memo-2012-02. "EUTelescope. Offline track reconstruction and DUT analysis software", 2012.

[36] Kyrre Ness Sjobak, "Full simulation of a test beam experiment including modeling of the Bonn Atlas Telescope and Atlas 3D pixel silicon sensors", University of Oslo 2010.

[37] G. Pellegrini, et al., "Nucl. Instrum. Methods Phys". Res. A 592, 38 (2008).

[38] ATLAS TWiki page, 3DTBAugust2012, https://twiki.cern.ch/twiki/bin/viewauth/Atlas/3DTBAugust2012, aval. June 2013.

[39] ATLAS TWiki page, AFPJune2013 , https://twiki.cern.ch/twiki/bin/viewauth/Atlas/AFPJune2013, aval. June 2013.